ϕ meson production in d+Au collisions at √sNN=200GeV

(PHENIX Collaboration) Adare, A.; ...; Makek, Mihael; ...; Zou, L.

Source / Izvornik: **Physical Review C - Nuclear Physics, 2015, 92**

Journal article, Published version
Rad u časopisu, Objavljena verzija rada (izdavačev PDF)

https://doi.org/10.1103/PhysRevC.92.044909

Permanent link / Trajna poveznica: https://urn.nsk.hr/urn:nbn:hr:217:182908

Rights / Prava: In copyright / Zaštićeno autorskim pravom.

Download date / Datum preuzimanja: **2024-04-25**

Repository / Repozitorij:

Repository of the Faculty of Science - University of Zagreb

ϕ meson production in d + Au collisions at $\sqrt{s_{NN}} = 200$ GeV

A. Adare,[13] C. Aidala,[42,43] N. N. Ajitanand,[62] Y. Akiba,[56,57] H. Al-Bataineh,[50] J. Alexander,[62] M. Alfred,[23] A. Angerami,[14] K. Aoki,[31,34,56] N. Apadula,[28,63] Y. Aramaki,[12,56] H. Asano,[34,56] E. T. Atomssa,[35] R. Averbeck,[63] T. C. Awes,[52] B. Azmoun,[7] V. Babintsev,[24] M. Bai,[6] G. Baksay,[19] L. Baksay,[19] N. S. Bandara,[42] B. Bannier,[63] K. N. Barish,[8] B. Bassalleck,[49] A. T. Basye,[1] S. Bathe,[5,8,57] V. Baublis,[55] C. Baumann,[7,44] A. Bazilevsky,[7] M. Beaumier,[8] S. Beckman,[13] S. Belikov,[7,*] R. Belmont,[43,67] R. Bennett,[63] A. Berdnikov,[59] Y. Berdnikov,[59] J. H. Bhom,[71] D. S. Blau,[33] J. S. Bok,[50,71] K. Boyle,[57,63] M. L. Brooks,[38] J. Bryslawskyj,[5] H. Buesching,[7] V. Bumazhnov,[24] G. Bunce,[7,57] S. Butsyk,[38] S. Campbell,[14,28,63] A. Caringi,[45] C.-H. Chen,[57,63] C. Y. Chi,[14] M. Chiu,[7] I. J. Choi,[25,71] J. B. Choi,[10] R. K. Choudhury,[4] P. Christiansen,[40] T. Chujo,[66] P. Chung,[62] O. Chvala,[8] V. Cianciolo,[52] Z. Citron,[63,69] B. A. Cole,[14] Z. Conesa del Valle,[35] M. Connors,[63] M. Csanád,[17] T. Csörgő,[70] T. Dahms,[63] S. Dairaku,[34,56] I. Danchev,[67] D. Danley,[51] K. Das,[20] A. Datta,[42,49] M. S. Daugherity,[1] G. David,[7] M. K. Dayananda,[21] K. DeBlasio,[49] K. Dehmelt,[63] A. Denisov,[24] A. Deshpande,[57,63] E. J. Desmond,[7] K. V. Dharmawardane,[50] O. Dietzsch,[60] A. Dion,[28,63] P. B. Diss,[41] J. H. Do,[71] M. Donadelli,[60] L. D'Orazio,[41] O. Drapier,[35] A. Drees,[63] K. A. Drees,[6] J. M. Durham,[38,63] A. Durum,[24] D. Dutta,[4] S. Edwards,[20] Y. V. Efremenko,[52] F. Ellinghaus,[13] T. Engelmore,[14] A. Enokizono,[52,56,58] H. En'yo,[56,57] S. Esumi,[66] B. Fadem,[45] N. Feege,[63] D. E. Fields,[49] M. Finger,[9] M. Finger, Jr.,[9] F. Fleuret,[35] S. L. Fokin,[33] Z. Fraenkel,[69,*] J. E. Frantz,[51,63] A. Franz,[7] A. D. Frawley,[20] K. Fujiwara,[56] Y. Fukao,[56] T. Fusayasu,[47] C. Gal,[63] P. Gallus,[15] P. Garg,[3] I. Garishvili,[37,64] H. Ge,[63] F. Giordano,[25] A. Glenn,[37] H. Gong,[63] M. Gonin,[35] Y. Goto,[56,57] R. Granier de Cassagnac,[35] N. Grau,[2,14] S. V. Greene,[67] G. Grim,[38] M. Grosse Perdekamp,[25] T. Gunji,[12] H.-Å. Gustafsson,[40,*] T. Hachiya,[56] J. S. Haggerty,[7] K. I. Hahn,[18] H. Hamagaki,[12] J. Hamblen,[64] H. F. Hamilton,[1] R. Han,[54] S. Y. Han,[18] J. Hanks,[14,63] S. Hasegawa,[29] T. O. S. Haseler,[21] K. Hashimoto,[56,58] E. Haslum,[40] R. Hayano,[12] X. He,[21] M. Heffner,[37] T. K. Hemmick,[63] T. Hester,[8] J. C. Hill,[28] M. Hohlmann,[19] R. S. Hollis,[8] W. Holzmann,[14] K. Homma,[22] B. Hong,[32] T. Horaguchi,[22] D. Hornback,[64] T. Hoshino,[22] N. Hotvedt,[28] J. Huang,[7] S. Huang,[67] T. Ichihara,[56,57] R. Ichimiya,[56] Y. Ikeda,[66] K. Imai,[29,34,56] M. Inaba,[66] A. Iordanova,[8] D. Isenhower,[1] M. Ishihara,[56] M. Issah,[67] D. Ivanishchev,[55] Y. Iwanaga,[22] B. V. Jacak,[63] M. Jezghani,[21] J. Jia,[7,62] X. Jiang,[38] J. Jin,[14] B. M. Johnson,[7] T. Jones,[1] K. S. Joo,[46] D. Jouan,[53] D. S. Jumper,[1,25] F. Kajihara,[12] J. Kamin,[63] S. Kanda,[12] J. H. Kang,[71] J. Kapustinsky,[38] K. Karatsu,[34,56] M. Kasai,[56,58] D. Kawall,[42,57] M. Kawashima,[56,58] A. V. Kazantsev,[33] T. Kempel,[28] J. A. Key,[49] V. Khachatryan,[63] A. Khanzadeev,[55] K. M. Kijima,[22] J. Kikuchi,[68] A. Kim,[18] B. I. Kim,[32] C. Kim,[32] D. J. Kim,[30] E.-J. Kim,[10] G. W. Kim,[18] M. Kim,[61] Y.-J. Kim,[25] B. Kimelman,[45] E. Kinney,[13] Á. Kiss,[17] E. Kistenev,[7] R. Kitamura,[12] J. Klatsky,[20] D. Kleinjan,[8] P. Kline,[63] T. Koblesky,[13] L. Kochenda,[55] B. Komkov,[55] M. Konno,[66] J. Koster,[25] D. Kotov,[55,59] A. Král,[15] A. Kravitz,[14] G. J. Kunde,[38] K. Kurita,[56,58] M. Kurosawa,[56,57] Y. Kwon,[71] G. S. Kyle,[50] R. Lacey,[62] Y. S. Lai,[14] J. G. Lajoie,[28] A. Lebedev,[28] D. M. Lee,[38] J. Lee,[18] K. B. Lee,[32] K. S. Lee,[32] S Lee,[71] S. H. Lee,[63] M. J. Leitch,[38] M. A. L. Leite,[60] X. Li,[11] P. Lichtenwalner,[45] P. Liebing,[57] S. H. Lim,[71] L. A. Linden Levy,[13] T. Liška,[15] H. Liu,[38] M. X. Liu,[38] B. Love,[67] D. Lynch,[7] C. F. Maguire,[67] Y. I. Makdisi,[6] M. Makek,[72] M. D. Malik,[49] A. Manion,[63] V. I. Manko,[33] E. Mannel,[7,14] Y. Mao,[54,56] H. Masui,[66] F. Matathias,[14] M. McCumber,[38,63] P. L. McGaughey,[38] D. McGlinchey,[13,20] C. McKinney,[25] N. Means,[63] A. Meles,[50] M. Mendoza,[8] B. Meredith,[25] Y. Miake,[66] T. Mibe,[31] A. C. Mignerey,[41] K. Miki,[56,66] A. Milov,[7,69] D. K. Mishra,[4] J. T. Mitchell,[7] S. Miyasaka,[56,65] S. Mizuno,[56,66] A. K. Mohanty,[4] P. Montuenga,[25] H. J. Moon,[46] T. Moon,[71] Y. Morino,[12] A. Morreale,[8] D. P. Morrison,[7,†] T. V. Moukhanova,[33] T. Murakami,[34,56] J. Murata,[56,58] A. Mwai,[62] S. Nagamiya,[31,56] K. Nagashima,[22] J. L. Nagle,[13,‡] M. Naglis,[69] M. I. Nagy,[17,70] I. Nakagawa,[56,57] H. Nakagomi,[56,66] Y. Nakamiya,[22] K. R. Nakamura,[34,56] T. Nakamura,[56] K. Nakano,[56,65] S. Nam,[18] C. Nattrass,[64] P. K. Netrakanti,[4] J. Newby,[37] M. Nguyen,[63] M. Nihashi,[22] T. Niida,[66] S. Nishimura,[12] R. Nouicer,[7,57] T. Novak,[70] N. Novitzky,[30,63] A. S. Nyanin,[33] C. Oakley,[21] E. O'Brien,[7] S. X. Oda,[12] C. A. Ogilvie,[28] M. Oka,[66] K. Okada,[57] Y. Onuki,[56] J. D. Orjuela Koop,[13] J. D. Osborn,[43] A. Oskarsson,[40] M. Ouchida,[22,56] K. Ozawa,[12,31] R. Pak,[7] V. Pantuev,[26,63] V. Papavassiliou,[50] I. H. Park,[18] J. S. Park,[61] S. Park,[61] S. K. Park,[32] W. J. Park,[32] S. F. Pate,[50] M. Patel,[28] H. Pei,[28] J.-C. Peng,[25] H. Pereira,[16] D. V. Perepelitsa,[7] G. D. N. Perera,[50] D.Yu. Peressounko,[33] J. Perry,[28] R. Petti,[7,63] C. Pinkenburg,[7] R. Pinson,[1] R. P. Pisani,[7] M. Proissl,[63] M. L. Purschke,[7] H. Qu,[21] J. Rak,[30] B. J. Ramson,[43] I. Ravinovich,[69] K. F. Read,[52,64] S. Rembeczki,[19] K. Reygers,[44] D. Reynolds,[62] V. Riabov,[48,55] Y. Riabov,[55,59] E. Richardson,[41] T. Rinn,[28] D. Roach,[67] G. Roche,[39,*] S. D. Rolnick,[8] M. Rosati,[28] C. A. Rosen,[13] S. S. E. Rosendahl,[40] Z. Rowan,[5] J. G. Rubin,[43] P. Ružička,[27] B. Sahlmueller,[44,63] N. Saito,[31] T. Sakaguchi,[7] K. Sakashita,[56,65] H. Sako,[29] V. Samsonov,[48,55] S. Sano,[12,68] M. Sarsour,[21] S. Sato,[29,31] T. Sato,[66] S. Sawada,[31] B. Schaefer,[67] B. K. Schmoll,[64] K. Sedgwick,[8] J. Seele,[13] R. Seidl,[25,56,57] A. Sen,[64] R. Seto,[8] P. Sett,[4] A. Sexton,[41] D. Sharma,[63,69] I. Shein,[24] T.-A. Shibata,[56,65] K. Shigaki,[22] M. Shimomura,[28,66] K. Shoji,[34,56] P. Shukla,[4] A. Sickles,[7,25] C. L. Silva,[28,38] D. Silvermyr,[40,52] C. Silvestre,[16] K. S. Sim,[32] B. K. Singh,[3] C. P. Singh,[3] V. Singh,[3] M. Slunečka,[9] M. Snowball,[38] R. A. Soltz,[37] W. E. Sondheim,[38] S. P. Sorensen,[64] I. V. Sourikova,[7] P. W. Stankus,[52] E. Stenlund,[40] M. Stepanov,[42,50,*] S. P. Stoll,[7] T. Sugitate,[22] A. Sukhanov,[7] T. Sumita,[56] J. Sun,[63] J. Sziklai,[70] E. M. Takagui,[60] A. Taketani,[56,57] R. Tanabe,[66] Y. Tanaka,[47] S. Taneja,[63] K. Tanida,[34,56,57,61] M. J. Tannenbaum,[7] S. Tarafdar,[3,69] A. Taranenko,[48,62] H. Themann,[63] D. Thomas,[1] T. L. Thomas,[49] R. Tieulent,[21] A. Timilsina,[28] T. Todoroki,[56,66] M. Togawa,[57] A. Toia,[63] L. Tomášek,[27] M. Tomášek,[15,27] H. Torii,[22] C. L. Towell,[1] R. Towell,[1] R. S. Towell,[1] I. Tserruya,[69] Y. Tsuchimoto,[22] C. Vale,[7] H. Valle,[67] H. W. van Hecke,[38] E. Vazquez-Zambrano,[14] A. Veicht,[14,25] J. Velkovska,[67] R. Vértesi,[70] M. Virius,[15] V. Vrba,[15,27] E. Vznuzdaev,[55] X. R. Wang,[50,57] D. Watanabe,[22] K. Watanabe,[66] Y. Watanabe,[56,57] Y. S. Watanabe,[12,31] F. Wei,[28,50] R. Wei,[62] J. Wessels,[44] A. S. White,[43] S. N. White,[7] D. Winter,[14] C. L. Woody,[7] R. M. Wright,[1] M. Wysocki,[13,52]

 ©2015 American Physical Society

B. Xia,[51] L. Xue,[21] S. Yalcin,[63] Y. L. Yamaguchi,[12,56,63] K. Yamaura,[22] R. Yang,[25] A. Yanovich,[24] J. Ying,[21] S. Yokkaichi,[56,57] J. H. Yoo,[32] I. Yoon,[61] Z. You,[54] G. R. Young,[52] I. Younus,[36,49] H. Yu,[54] I. E. Yushmanov,[33] W. A. Zajc,[14] A. Zelenski,[6] S. Zhou,[11] and L. Zou[8]

(PHENIX Collaboration)

[1]*Abilene Christian University, Abilene, Texas 79699, USA*
[2]*Department of Physics, Augustana College, Sioux Falls, South Dakota 57197, USA*
[3]*Department of Physics, Banaras Hindu University, Varanasi 221005, India*
[4]*Bhabha Atomic Research Centre, Bombay 400 085, India*
[5]*Baruch College, City University of New York, New York, New York 10010, USA*
[6]*Collider-Accelerator Department, Brookhaven National Laboratory, Upton, New York 11973-5000, USA*
[7]*Physics Department, Brookhaven National Laboratory, Upton, New York 11973-5000, USA*
[8]*University of California-Riverside, Riverside, California 92521, USA*
[9]*Charles University, Ovocný trh 5, Praha 1, 116 36, Prague, Czech Republic*
[10]*Chonbuk National University, Jeonju 561-756, Korea*
[11]*Science and Technology on Nuclear Data Laboratory, China Institute of Atomic Energy, Beijing 102413, People's Republic of China*
[12]*Center for Nuclear Study, Graduate School of Science, University of Tokyo, 7%–3%–1 Hongo, Bunkyo, Tokyo 113-0033, Japan*
[13]*University of Colorado, Boulder, Colorado 80309, USA*
[14]*Columbia University, New York, New York 10027, USA and Nevis Laboratories, Irvington, New York 10533, USA*
[15]*Czech Technical University, Zikova 4, 166 36 Prague 6, Czech Republic*
[16]*Dapnia, CEA Saclay, F-91191, Gif-sur-Yvette, France*
[17]*ELTE, Eötvös Loránd University, Pázmány P. s. 1/A, H-1117 Budapest, Hungary*
[18]*Ewha Womans University, Seoul 120-750, Korea*
[19]*Florida Institute of Technology, Melbourne, Florida 32901, USA*
[20]*Florida State University, Tallahassee, Florida 32306, USA*
[21]*Georgia State University, Atlanta, Georgia 30303, USA*
[22]*Hiroshima University, Kagamiyama, Higashi-Hiroshima 739-8526, Japan*
[23]*Department of Physics and Astronomy, Howard University, Washington, DC 20059, USA*
[24]*IHEP Protvino, State Research Center of Russian Federation, Institute for High Energy Physics, Protvino 142281, Russia*
[25]*University of Illinois at Urbana-Champaign, Urbana, Illinois 61801, USA*
[26]*Institute for Nuclear Research of the Russian Academy of Sciences, prospekt 60-letiya Oktyabrya 7a, Moscow 117312, Russia*
[27]*Institute of Physics, Academy of Sciences of the Czech Republic, Na Slovance 2, 182 21 Prague 8, Czech Republic*
[28]*Iowa State University, Ames, Iowa 50011, USA*
[29]*Advanced Science Research Center, Japan Atomic Energy Agency, 2-4 Shirakata Shirane, Tokai-mura, Naka-gun, Ibaraki-ken 319-1195, Japan*
[30]*Helsinki Institute of Physics and University of Jyväskylä, P.O. Box 35, FI-40014 Jyväskylä, Finland*
[31]*KEK, High Energy Accelerator Research Organization, Tsukuba, Ibaraki 305-0801, Japan*
[32]*Korea University, Seoul 136-701, Korea*
[33]*Russian Research Center "Kurchatov Institute," Moscow 123098, Russia*
[34]*Kyoto University, Kyoto 606-8502, Japan*
[35]*Laboratoire Leprince-Ringuet, Ecole Polytechnique, CNRS-IN2P3, Route de Saclay, F-91128, Palaiseau, France*
[36]*Physics Department, Lahore University of Management Sciences, Lahore 54792, Pakistan*
[37]*Lawrence Livermore National Laboratory, Livermore, California 94550, USA*
[38]*Los Alamos National Laboratory, Los Alamos, New Mexico 87545, USA*
[39]*LPC, Université Blaise Pascal, CNRS-IN2P3, Clermont-Fd, 63177 Aubiere Cedex, France*
[40]*Department of Physics, Lund University, Box 118, SE-221 00 Lund, Sweden*
[41]*University of Maryland, College Park, Maryland 20742, USA*
[42]*Department of Physics, University of Massachusetts, Amherst, Massachusetts 01003-9337, USA*
[43]*Department of Physics, University of Michigan, Ann Arbor, Michigan 48109-1040, USA*
[44]*Institut für Kernphysik, University of Muenster, D-48149 Muenster, Germany*
[45]*Muhlenberg College, Allentown, Pennsylvania 18104-5586, USA*
[46]*Myongji University, Yongin, Kyonggido 449-728, Korea*
[47]*Nagasaki Institute of Applied Science, Nagasaki-shi, Nagasaki 851-0193, Japan*
[48]*National Research Nuclear University, MEPhI, Moscow Engineering Physics Institute, Moscow 115409, Russia*
[49]*University of New Mexico, Albuquerque, New Mexico 87131, USA*
[50]*New Mexico State University, Las Cruces, New Mexico 88003, USA*
[51]*Department of Physics and Astronomy, Ohio University, Athens, Ohio 45701, USA*
[52]*Oak Ridge National Laboratory, Oak Ridge, Tennessee 37831, USA*
[53]*IPN-Orsay, Universite Paris Sud, CNRS-IN2P3, BP1, F-91406, Orsay, France*

[54] *Peking University, Beijing 100871, People's Republic of China*
[55] *PNPI, Petersburg Nuclear Physics Institute, Gatchina, Leningrad region, 188300, Russia*
[56] *RIKEN Nishina Center for Accelerator-Based Science, Wako, Saitama 351-0198, Japan*
[57] *RIKEN BNL Research Center, Brookhaven National Laboratory, Upton, New York 11973-5000, USA*
[58] *Physics Department, Rikkyo University, 3-34-1 Nishi-Ikebukuro, Toshima, Tokyo 171-8501, Japan*
[59] *Saint Petersburg State Polytechnic University, St. Petersburg, 195251 Russia*
[60] *Universidade de São Paulo, Instituto de Física, Caixa Postal 66318, São Paulo CEP05315-970, Brazil*
[61] *Department of Physics and Astronomy, Seoul National University, Seoul 151-742, Korea*
[62] *Chemistry Department, Stony Brook University, SUNY, Stony Brook, New York 11794-3400, USA*
[63] *Department of Physics and Astronomy, Stony Brook University, SUNY, Stony Brook, New York 11794-3800, USA*
[64] *University of Tennessee, Knoxville, Tennessee 37996, USA*
[65] *Department of Physics, Tokyo Institute of Technology, Oh-okayama, Meguro, Tokyo 152-8551, Japan*
[66] *Institute of Physics, University of Tsukuba, Tsukuba, Ibaraki 305, Japan*
[67] *Vanderbilt University, Nashville, Tennessee 37235, USA*
[68] *Waseda University, Advanced Research Institute for Science and Engineering, 17 Kikui-cho, Shinjuku-ku, Tokyo 162-0044, Japan*
[69] *Weizmann Institute, Rehovot 76100, Israel*
[70] *Institute for Particle and Nuclear Physics, Wigner Research Centre for Physics, Hungarian Academy of Sciences (Wigner RCP, RMKI) H-1525 Budapest 114, P.O. Box 49, Budapest, Hungary*
[71] *Yonsei University, IPAP, Seoul 120-749, Korea*
[72] *University of Zagreb, Faculty of Science, Department of Physics, Bijenička 32, HR-10002 Zagreb, Croatia*
(Received 30 June 2015; published 19 October 2015)

The PHENIX Collaboration has measured ϕ meson production in d + Au collisions at $\sqrt{s_{NN}} = 200$ GeV using the dimuon and dielectron decay channels. The ϕ meson is measured in the forward (backward) d-going (Au-going) direction, $1.2 < y < 2.2$ ($-2.2 < y < -1.2$) in the transverse-momentum (p_T) range from 1–7 GeV/c and at midrapidity $|y| < 0.35$ in the p_T range below 7 GeV/c. The ϕ meson invariant yields and nuclear-modification factors as a function of p_T, rapidity, and centrality are reported. An enhancement of ϕ meson production is observed in the Au-going direction, while suppression is seen in the d-going direction, and no modification is observed at midrapidity relative to the yield in $p + p$ collisions scaled by the number of binary collisions. Similar behavior was previously observed for inclusive charged hadrons and open heavy flavor, indicating similar cold-nuclear-matter effects.

DOI: 10.1103/PhysRevC.92.044909 PACS number(s): 25.75.Dw

I. INTRODUCTION

Collisions of deuterons with gold nuclei (d + Au) are of significant interest in the study of the strongly coupled quark gluon plasma (QGP) produced at the BNL Relativistic Heavy Ion Collider (RHIC) [1,2]. The highly asymmetric collisions of a small projectile and a large target nucleus provide a way to investigate the initial state of a nucleus-nucleus collision experimentally, potentially disentangling effects owing to QGP formation from the cold-nuclear-matter effects. The latter include modification of the parton distribution functions (PDFs) in the nucleus relative to those in the nucleon [3], initial-state energy loss [4], and the so-called Cronin effect. The Cronin effect refers to the enhancement of high-p_T particle production in $p + A$ collisions relative to that in $p + p$ collisions scaled by the number of binary collisions and is often attributed to multiple scattering of the incoming parton inside the target nucleus [5,6]. In addition, results from recent $p(d) + A$ collisions at the CERN Large Hadron Collider and RHIC suggest that long-range correlations, either present in the initial state or induced by the evolution of the medium, play an important role even in these small collision systems [7–20]. Detailed studies of particle-production systematics in d + Au at RHIC may inform this question [21–26].

PHENIX has measured the production of identified particles, such as π, K, and p, at midrapidity in d + Au and Au + Au collisions and has found intriguing similarities between the K/π and p/π ratios in peripheral Au + Au and central d + Au collisions [24]. However, it was observed that the ratio of spectra in peripheral Au + Au to those in central d + Au starts above 1 at low-p_T and trends to a constant value of ~0.65 for all identified particles at high p_T. One explanation for the low-p_T rise is a relative deficit of midrapidity soft-particle yield in d + Au collisions compared to Au + Au, which could be attributable to the participant asymmetry in the d + Au collisions producing a rapidity shift in the peak of particle production [9]. Consequently, measuring identified particles in different regions of rapidity provides a more complete picture of d + Au collisions and sheds light on the relationship between $p + p$, d + Au, and Au + Au. Measuring identified particle production at forward rapidity also enables access to the low-x region, where nuclear PDFs (nPDFs) are not well known and where one expects

*Deceased
†PHENIX cospokesperson: morrison@bnl.gov
‡PHENIX cospokesperson: jamie.nagle@colorado.edu

parton-saturation effects to begin to manifest in modified particle production.

The yield of ϕ mesons in high-energy heavy-ion collisions provides key information about the QGP, as the yield is potentially sensitive to medium-induced effects such as strangeness enhancement [27], a phenomenon associated with soft particles in bulk matter which can be accessed through the measurements of ϕ meson production [28–37]. PHENIX measures ϕ meson production over a wide rapidity range and for various collision systems such as $p+p$, $d+\mathrm{Au}$, and $\mathrm{Au}+\mathrm{Au}$. The production of ϕ mesons has already been measured in $p+p$, $d+\mathrm{Au}$, $\mathrm{Cu}+\mathrm{Cu}$, and $\mathrm{Au}+\mathrm{Au}$ at midrapidity [30,36,38] and in $p+p$ at forward and backward rapidities [39] over a wide range in p_T.

In this paper, the production of ϕ mesons is determined at forward and backward rapidities via dimuons detected in the PHENIX muon spectrometers and at midrapidity via dielectrons detected in the PHENIX central arms. Measurements of the ϕ meson nuclear-modification factor ($R_{d\mathrm{Au}}$) in $d+\mathrm{Au}$ collisions versus rapidity and versus p_T are presented. The results presented here are based on $d+\mathrm{Au}$ collisions at $\sqrt{s_{NN}} = 200$ GeV recorded in 2008. The luminosity used in $\phi \to \mu^+\mu^-$ analysis corresponds to 60 nb^{-1}, which is equivalent to a nucleon-nucleon integrated luminosity of 24 pb^{-1}, while the luminosity used in $\phi \to e^+e^-$ analysis corresponds to 71 nb^{-1}, which is equivalent to a nucleon-nucleon integrated luminosity of 28 pb^{-1}.

II. EXPERIMENT

Figure 1 shows a schematic of the PHENIX detector, which is described in detail in Ref. [40]. The detectors relevant for the analysis of the ϕ meson in the dilepton channels are the central arms, two muon spectrometers, and the two beam-beam counters.

The PHENIX central arms measure particles by using drift chambers (DCs) and pad chambers for the tracking and momentum measurement of charged particles, ring imaging Čerenkov detectors (RICHs) for the separation of electrons up to the π meson Čerenkov radiation threshold at 5 GeV/c, and an electromagnetic calorimeter (EMCal) for the measurement of spatial positions and energies of photons and electrons. The EMCal comprises six sectors of lead-scintillator calorimeter and two sectors of lead-glass calorimeter.

The muon spectrometers, located at forward and backward rapidities, are shielded by absorbers composed of 19 cm of copper and 60 cm of iron. Each spectrometer comprises the muon tracker (MuTr) immersed in a radial magnetic field of integrated bending power of 0.8 T m and backed by the muon identifier (MuID). The muon spectrometers subtend $1.2 < |\eta| < 2.2$ and the full azimuth. The MuTr comprises three sets of cathode strip chambers while the MuID comprises five planes of Iarocci tubes interleaved with steel absorber plates. The momentum resolution, $\delta p/p$, of particles in the analyzed momentum range is about 5%, independent of momentum and dominated by multiple scattering. Muon candidates are identified by matching tracks reconstructed in the MuTr to MuID tracks that penetrate through to the last MuID plane.

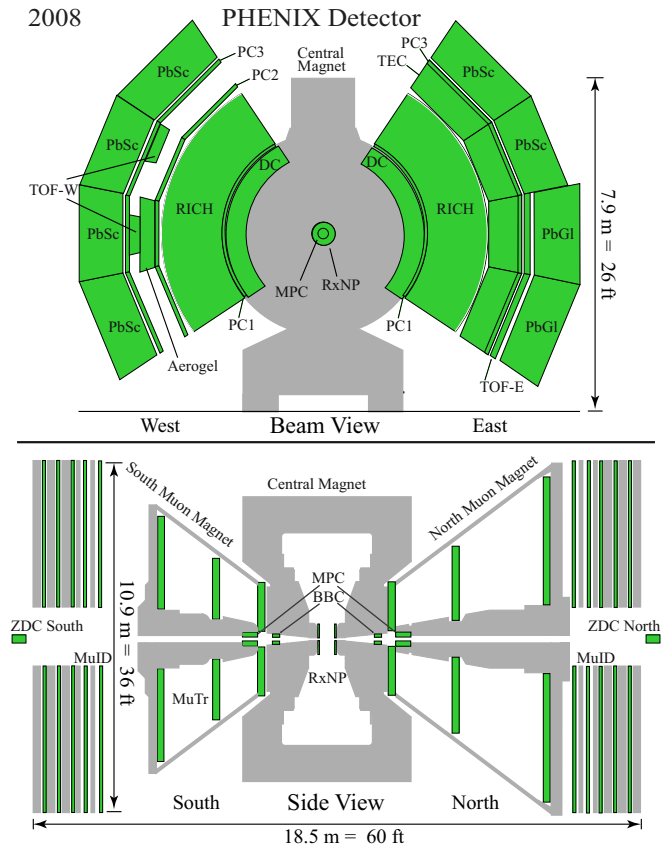

FIG. 1. (Color online) A schematic side view of the PHENIX detector configuration in the 2008 data-taking period.

The minimum momentum of a muon to reach the last MuID plane is $\sim 2\,\mathrm{GeV}/c$.

Beam-beam counters (BBCs), comprising two arrays of 64 Čerenkov counters covering the pseudorapidity range $3.1 < |\eta| < 3.9$, measure the collision vertex along the beam axis (z_{vtx}) with 0.5 cm resolution in addition to providing a minimum-bias (MB) trigger.

III. DATA ANALYSIS

This section describes the details of the measurement of the ϕ meson in $\phi \to \mu^+\mu^-$ and $\phi \to e^+e^-$ decay channels.

A. $\phi \to \mu^+\mu^-$ measurement

The dimuon data set for this analysis was collected in 2008 using a MB trigger that requires at least one hit in each of the BBC detectors in conjunction with the MuID Level-1 dimuon trigger. Also, at least two tracks were required to penetrate to the last layer of the MuID. The MB trigger measures $88\% \pm 4\%$ of the total $d+\mathrm{Au}$ inelastic cross section of 2260 mb [21].

A set of cuts was employed to select good muon candidates and improve the signal-to-background ratio. Event selection requires the BBC collision z vertex to be reconstructed within ± 30 cm of the center of the interaction region along the beam axis. The MuTr tracks are matched to the MuID tracks at

the first MuID layer in both position and angle. The track is required to have at least 8 of 10 possible hits in the MuID.

The invariant mass distribution is formed by combining muon candidate tracks of opposite charge. In addition to low-mass vector mesons, the invariant mass spectra in the region of interest contain uncorrelated and correlated backgrounds. The uncorrelated backgrounds arise from random combinatoric associations of unrelated muon candidates while the correlated backgrounds arise from open charm decay (e.g., $D\bar{D}$ where both mesons decay semileptonically to muons), open bottom decay, η and ω Dalitz decays, and the Drell-Yan process. The correlated background is much smaller than the uncorrelated background for all centralities. It is also established from simulation that the background is dominated by the uncorrelated contribution from decays, such as $K,\pi \to \mu\nu$, that occur in front of and inside the absorber. A smaller contribution to the background comes from hadron decays in the MuTr volume. When combined into track pairs, these pairs produce a broad distribution of invariant masses and also a broad distribution of $\chi^2_{\rm vtx}$, the parameter resulting from fitting the two muon tracks with the BBC measured event vertex position. This procedure separates the foreground and background spectra by applying a cut of $\chi^2_{\rm vtx} < 4.0$ to extract foreground spectra and a cut of $\chi^2_{\rm vtx} > 4.0$ to extract background spectra. The cut value, $\chi^2_{\rm vtx,cut} = 4.0$, is selected such that it retains as much of the signal as possible within the foreground, while still allowing sufficient statistics in the background sample. This procedure is described in detail in Ref. [39].

To extract the ϕ meson signal, the background pairs are subtracted from the foreground pairs. Because the pairs with $\chi^2_{\rm vtx} > 4.0$ represent only the uncorrelated part of the background, the shape of their mass distribution is slightly altered to account for the contribution of correlated pairs, which have much smaller contribution according to simulation results. This is done by fitting a fourth-order polynomial to the ratio of the foreground to background distributions in the nonresonance region ($0.3 < M_{\mu^+\mu^-} < 0.5$ GeV/c^2 and $1.5 < M_{\mu^+\mu^-} < 2.5$ GeV/c^2). The background distribution is then multiplied by the polynomial in the entire mass range. Figure 2 shows the resulting foreground and renormalized background distributions.

In the mass range $0.3 < M_{\mu^+\mu^-} < 2.5$ GeV/c^2, the resulting distribution after background subtraction has contributions from three mesons: ω, ρ, and ϕ mesons. The distribution is fitted with the sum of two Gaussian functions and the Breit-Wigner function convoluted with a Gaussian. The Gaussian functions are used to fit the ω and ϕ mesons, while the Breit-Wigner convoluted with a Gaussian is used to fit the ρ meson. Figure 3 shows the results.

The parameters of the fit are fixed to the world average values of the masses and widths of the three mesons [41] and the widths of the Gaussian distributions, which account for the detector mass resolution, are constrained by the values obtained from the simulation. The ϕ meson mass resolution is $\sim$85 MeV/c^2. Because the invariant mass peak of the ϕ meson is partly resolved in the plot, while ω and ρ meson peaks cannot be resolved, only an estimate of the combined yield of these two mesons is allowed. In the fit, the ratio of the ω and ρ mesons, N_ρ/N_ω, is set to 0.58, derived as

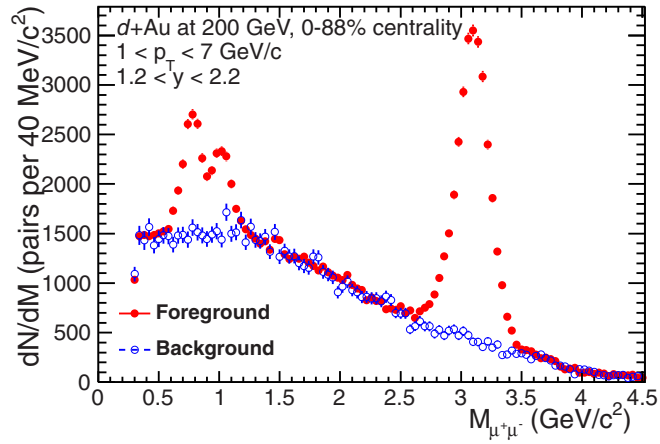

FIG. 2. (Color online) The unlike-sign dimuon invariant mass spectrum (solid red points) and the renormalized background spectrum (open blue circles).

the ratio of their corresponding production cross sections, $\sigma_\rho/\sigma_\omega = 1.15 \pm 0.15$, consistent with values found in jet fragmentation [42], multiplied by the ratio of their branching ratios [41].

The yield extraction is performed in bins of p_T over the range $1 < p_T < 7$ GeV/c for the rapidities $1.2 < |y| < 2.2$, in bins of y for the p_T range $1 < p_T < 7$ GeV/c, and in different centrality classes.

The acceptance and reconstruction efficiency ($A\varepsilon_{\rm rec}$) of the muon spectrometers, including the MuID trigger efficiency, is determined by passing PYTHIA 6.421 (default parameters) [43] generated ϕ mesons through a full GEANT [44] simulation of the PHENIX detector. The PYTHIA simulation output is embedded into real d + Au data events and then reconstructed in the same manner as data. Identical cuts to those used in the data analysis are applied to this embedded simulation.

Figure 4 shows the $A\varepsilon_{\rm rec}$ as a function of p_T and rapidity for ϕ mesons. The $A\varepsilon_{\rm rec}$ reaches a few percent at high-p_T and rapidly decreases at low momentum, limiting this study to $p_T > 1$ GeV/c.

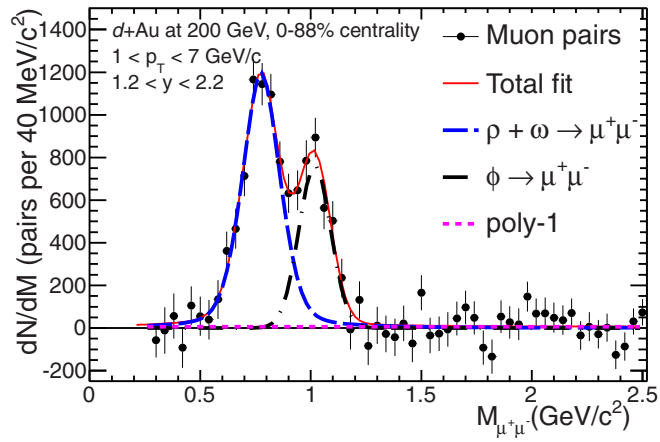

FIG. 3. (Color online) The fitted unlike-sign dimuon spectrum after background subtraction.

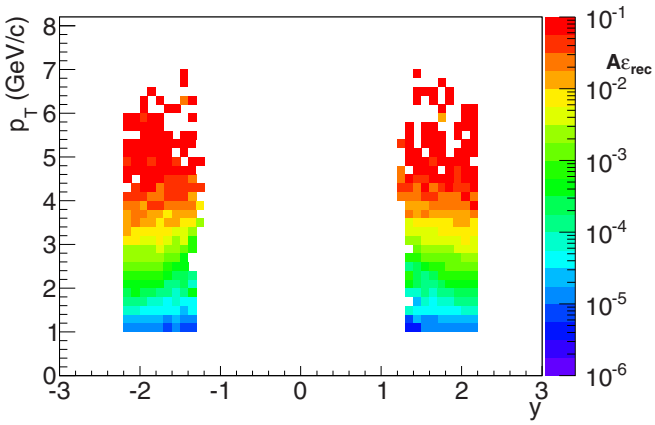

FIG. 4. (Color online) The $A\varepsilon_{\rm rec}$ as a function of rapidity (x axis) and p_T (y axis) for ϕ mesons.

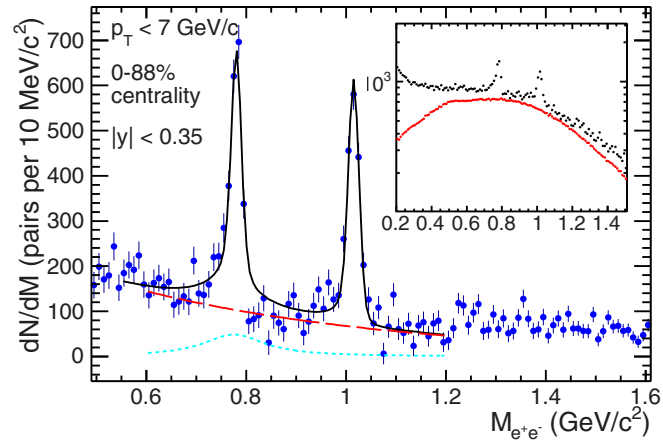

FIG. 5. (Color online) p_T-integrated unlike-sign e^+e^- mass spectrum measured by the PHENIX central arms after subtracting the uncorrelated combinatorial background in the MB $d+$Au collisions. The dotted line shows the ρ meson contribution and the dashed line is the polynomial background, which describes the residual correlated background. The inset shows the raw spectrum before subtraction, overlaid with the normalized combinatorial background, which is estimated using the mixed-event technique.

B. $\phi \to e^+e^-$ measurement

The dielectron data set for this analysis was recorded in 2008 using a MB trigger that required at least one hit in each of the BBC detectors with an ERT (EMCal-RICH trigger). The ERT requires a minimum energy deposit of 0.6 and 0.8 GeV/c in a tile of 2×2 EMCal towers matched to a hit in the RICH. The trigger efficiencies are described in detail in Ref. [45].

A set of quality-assurance cuts is applied to the data to select good electron candidates and improve the signal-to-background ratio. Event selection requires the BBC collision z vertex to be reconstructed within ± 30 cm of the center of the interaction region along the beam direction. Charged tracks are reconstructed using the DC and pad chambers and requiring $p_T > 0.2$ GeV/c. Electrons are identified mainly by the RICH detector. Furthermore, an electron candidate is required to have a good match to a cluster in the EMCal, and the energy, E, of the cluster must satisfy the requirement $E/p > 0.5$, where p is the momentum measured by the DCs. The RICH and EMCal combined provide an e/π rejection factor of order 10^4.

Electrons and positrons reconstructed in an event are combined into pairs. The resulting mass spectrum contains both the signal and an inherent background. The uncorrelated part of the background is estimated via an event-mixing technique [46], which combines electrons from different events within the same centrality and vertex class. To extract the ϕ meson raw yield, the subtracted mass spectrum is fitted by a function consisting of several contributions. The ϕ and ω meson peaks are approximated by a Breit-Wigner distribution convolved with a Gaussian distribution. Parameters of the Breit-Wigner part are set to the global averaged values [41] and the width of the Gaussian part is to account for the detector mass resolution. Because the production ratio of ρ meson to ω meson is assumed to be 1.15, their ratio in the fit is given by the ratio of their branching ratios to e^+e^- in vacuum. The ϕ meson yield is then extracted by summing up the bin contents in a $\pm 3\sigma$ window, where σ is extracted from the fit, and subtracting the background determined by integrating the polynomial over the same window.

Figure 5 shows an example of the fit to the mixed-event-subtracted mass spectrum. The mixed events were normalized in the mass range between 0.7 and 1.5 GeV/c^2. The stability of the results was checked by varying the normalization region, and the difference was included in the systematic uncertainties. The ratio of real to normalized mixed events was found to be flat in the region of interest for this analysis, indicating the validity of the normalization. Complete details describing the estimation of the systematic uncertainty on the raw yield extraction by varying the background normalization, fitting functions, range, and counting method can be found in Ref. [45].

The detector acceptance and reconstruction efficiency, as well as trigger efficiency were determined using a GEANT [44] based simulation of the PHENIX detector that tuned the detector response to a set of characteristics (dead and hot channel maps, gains, noise, etc.) that described the performance of each detector subsystem. The $\phi \to e^+e^-$ decays were generated with a realistic p_T distribution of ϕ mesons, within $|y| < 0.5$ in rapidity, and in full azimuth. The simulated ϕ meson mean and width of the invariant mass peak were verified to match the measured values in real data at all p_T. More details are given in Ref. [38].

C. Calculation of invariant yields and nuclear-modification factors

The dilepton ϕ meson invariant yield in a given rapidity, p_T, and centrality bin is

$$\frac{B_{ll}}{2\pi p_T}\frac{d^2N}{dy dp_T} = \frac{1}{2\pi p_T}\frac{1}{\Delta y \Delta p_T}\frac{cN_\phi}{\varepsilon_{\rm tot} N_{\rm evt}}, \qquad (1)$$

where B_{ll} is the $\phi \to l^+l^-$ branching ratio, N_ϕ is the measured ϕ meson yield, $N_{\rm evt}$ is the number of sampled MB events in the given centrality bin, Δy is the width of the rapidity bin, Δp_T is the width of the p_T bin, and c is the BBC bias correction factor [21,47]. $\varepsilon_{\rm tot}$ includes trigger efficiencies, acceptance, and reconstruction efficiency [45,48]. The data points are

corrected to account for the finite width of the analyzed p_T bins [49].

To gain insight into nuclear medium effects and particle-production mechanisms in d + Au collisions, the ratio of the ϕ meson yields in d + Au collisions to $p + p$ collisions scaled by the number of nucleon-nucleon collisions in the d + Au system, $N_{\rm coll}$ [21], is calculated as

$$R_{d\rm Au} = \frac{d^2N_{d\rm Au}/dydp_T}{N_{\rm coll} \times d^2N_{pp}/dydp_T}, \quad (2)$$

where $d^2N_{d\rm Au}/dydp_T$ is the per-event yield of particle production in d + Au collisions and $d^2N_{pp}/dydp_T$ is the per-event yield of the same process in $p + p$ collisions. The $p + p$ invariant yield used in the $R_{d\rm Au}$ calculation for the $\mu^+\mu^-$ decay channel is the $p + p$ differential cross section from Ref. [39] divided by the $p + p$ total cross section, 42.2 mb. The measured $p + p$ differential cross sections for e^+e^- and K^+K^- decay channels are consistent [38] and the $p + p$ reference used in the e^+e^- $R_{d\rm Au}$ calculations is extracted from a Tsallis function fit of the combined e^+e^- and K^+K^- spectra.

D. Systematic uncertainties

The systematic uncertainties associated with the measured invariant yields and nuclear-modification factors can be divided into three categories based upon the effect each source has on the measured results. All uncertainties are reported as standard deviations: type A, point-to-point uncorrelated uncertainties that allow the data points to move independently with respect to one another and are added in quadrature with statistical uncertainties; type B, point-to-point correlated uncertainties that allow the data points to move coherently within the quoted range; type C, correlated uncertainties that allow the data points to move together by a common multiplicative factor, a global uncertainty.

At forward and backward rapidities, a 5% type-A uncertainty is assigned to signal extraction, which corresponds to the average variation between the results from the different yield extraction fits. Type-B uncertainties, point-to-point correlated uncertainties to some degree in p_T, include a 4% uncertainty from MuID tube efficiency and 2% from MuTr overall efficiency. An 8% uncertainty on the yield is assigned to account for a 2% absolute momentum scale uncertainty, which was estimated by measuring the J/ψ mass.

A 9% (8%) uncertainty is assigned to the $-2.2 < y < -1.2$ ($1.2 < y < 2.2$) rapidity bins owing to the uncertainties in the $A\varepsilon_{\rm rec}$ determination method itself. The $A\varepsilon_{\rm rec}$ at the lowest p_T bin is small and sensitive to variations in the slope of the input p_T distribution, which affects the differential cross section calculations at this p_T bin. To understand this effect, the p_T-dependent cross section is fitted by three commonly used fit functions (Hagedorn [50], Kaplan *et al.* [51], and Tsallis [52], as used in Adare *et al.* [38]) over the p_T range, $2 < p_T < 7$ GeV/c, and the fitted functions are extrapolated to the lowest p_T bin, $1 < p_T < 2$ GeV/c. The differences between the values extracted from these fits and the measured one at the lowest p_T bin is within 8%; hence, an additional 8% systematic uncertainty is assigned to the lowest p_T bin to account for these differences. For the p_T-integrated and rapidity-dependent invariant yields, the 8% uncertainty is assigned to all data bins. Type-B systematic uncertainties are added in quadrature and are shown as boxes. Finally, an overall normalization uncertainty of 10% (0.1%–5.8%) for $p + p$ (d + Au) is assigned to the BBC bias correction (c) uncertainties and are labeled as type C [23]. The BBC bias correction uncertainties for d + Au vary with centrality and are considered as type B for centrality-dependent spectra.

TABLE I. Systematic uncertainties included in the invariant yield and the nuclear-modification-factor calculations at forward and backward rapidities. As explained in the text, there is an 8% type-B systematic uncertainty owing to small acceptance that impacts the low-p_T region only, which is not listed below.

Source	Value (%)	Type
Signal extraction	5	A
MuID efficiency	4	B
MuTr efficiency	2	B
$A\varepsilon_{\rm rec}$ (north/south)	8/9	B
Absolute momentum scale	8	B
Total type-B	13	B
BBC bias correction for $p + p$ (d + Au)	10 (0.1–5.8)	C
$N_{\rm coll}$	5–7	C

For the nuclear-modification factor, the type-A systematic uncertainties arise from the quadratic sum of type-A systematic uncertainty in $p + p$ and d + Au invariant yields [39]. Systematic uncertainties including MuID and MuTr efficiencies and absolute momentum scale are the same between the d + Au and $p + p$ invariant yields and cancel out. A 9% (7%) systematic uncertainty in the $A\varepsilon_{\rm rec}$ at $-2.2 < y < -1.2$ ($1.2 < y < 2.2$), which is carried over from $p + p$, is added in quadrature to type-B systematic uncertainties listed in Table I. The acceptance limitation at the lowest p_T bin is the same between d + Au and $p + p$ data because it is collected using the same detector and the associated type-B systematic uncertainty cancels out. Type-C systematic uncertainties for the nuclear-modification factor are the quadratic sum of the type-C systematic uncertainties for the invariant yields of $p + p$ and d + Au collisions and the uncertainty associated with $N_{\rm coll}$. The systematic uncertainties are listed in Table I.

At midrapidity, the main contribution to the systematic uncertainties of type-A is the uncertainty associated with the raw yield extraction, 8%–15%. This uncertainty is calculated by varying the background normalization, fitting functions, range, and counting methods. Type-B systematic uncertainties, point-to-point correlated uncertainties in p_T, include uncertainties in the ERT trigger efficiency (1%–7%) and electron identification (9%), which are estimated by varying the analysis cuts. The acceptance correction uncertainty is 7% and the momentum scale uncertainty is 1%–5%. An overall normalization uncertainty, type C, was assigned for the $p + p$ (d + Au) BBC bias correction, which amounts to 10% (0.1%–5.8%).

For the nuclear-modification factor, the electron identification and branching ratio uncertainties are the same between $p + p$ and d + Au and cancel out. As for the rest of the systematic uncertainties, the uncertainties for each type are

TABLE II. Systematic uncertainties included in the invariant yield and the nuclear-modification-factor calculations at midrapidity.

Source	Value (%)	Type
Signal extraction	8–15	A
ERT trigger efficiency	1–7	B
Acceptance correction	7	B
Electron ID	9	B
Absolute momentum scale	1–5	B
Quadratic sum of (B)	11–14	B
BBC bias correction for $p+p$ ($d+$Au)	10 (0.1–5.8)	C
$N_{\rm coll}$	5–7	C

added in quadrature between $p+p$ and $d+$Au. Additionally, the $N_{\rm coll}$ uncertainty is added in quadrature to the rest of type-C uncertainties. The systematic uncertainties are listed in Table II.

IV. RESULTS

Figure 6 shows the ϕ meson invariant yields in $d+$Au and $p+p$ as a function of p_T in the Au-going direction $-2.2 < y < -1.2$, in the d-going direction $1.2 < y < 2.2$, and at midrapidity $|y| < 0.35$. The invariant yields measured at forward and backward rapidities for all centralities are significantly different from each other. At midrapidity, the magnitude of the invariant yield is close to that of the backward rapidity, in contrast to what was observed in $p+p$ collisions [38], where the forward and backward rapidities have the same invariant yields and both are smaller than the midrapidity invariant yield.

Figure 7 shows the invariant yields as a function of p_T for the different centrality intervals measured in $p+p$ and $d+$Au collisions. The $d+$Au data are presented in different centrality classes—0%–20%, 20%–40%, 40%–60%, and 60%–88%, which are determined using the BBC over the pseudorapidity range $3.1 < |\eta| < 3.9$ for the $1.2 < |y| < 2.2$ and $|y| < 0.35$ regions. The three panels describe the three rapidity regions. The same centrality definition is used as in Ref. [47]. The wide rapidity coverage of the full PHENIX detector over an extended p_T range is demonstrated.

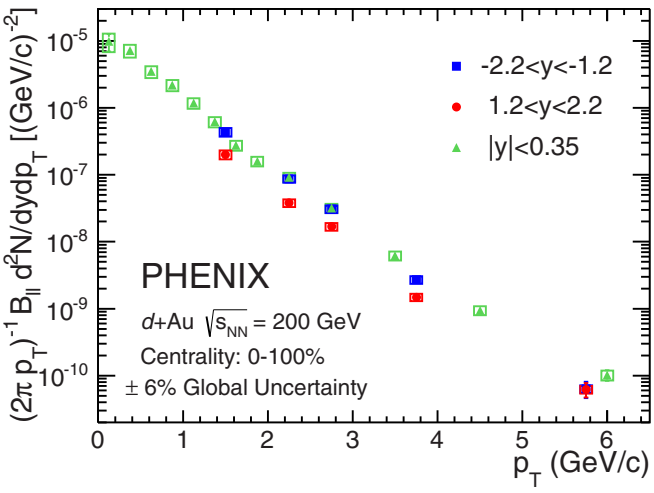

FIG. 6. (Color online) ϕ meson invariant yields as a function of p_T in the Au-going direction (solid blue squares) and in the d-going direction (solid red points). The ϕ meson invariant yields at midrapidity are shown as solid green triangles. The vertical bars represent the statistical uncertainties and the boxes represent type-B systematic uncertainties. The ±6% global uncertainty is the associated type-C uncertainty.

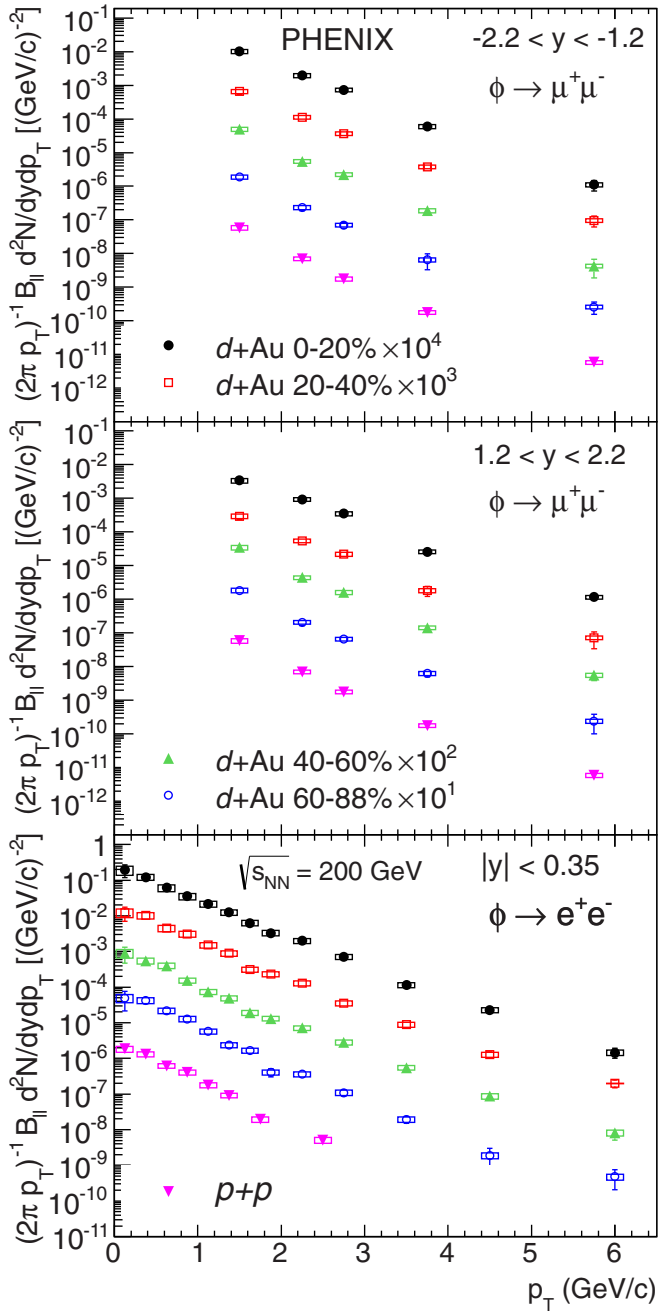

FIG. 7. (Color online) Invariant p_T spectra of the ϕ meson for different centrality classes in $d+$Au and $p+p$ collisions at $\sqrt{s_{NN}} =$ 200 GeV [39]. The vertical bars represent the statistical uncertainties and the boxes represent type-B systematic uncertainties. Type-C systematic uncertainties are 0.1%–5.8% for $d+$Au invariant yields and 10% for $p+p$ invariant yields. The spectra are scaled by arbitrary factors for clarity.

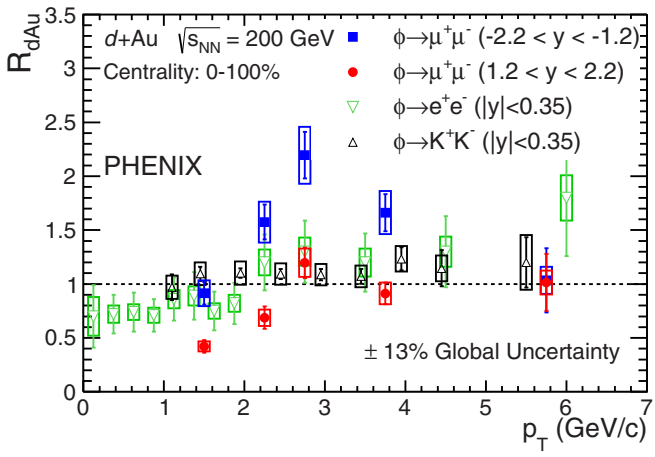

FIG. 8. (Color online) The ϕ meson nuclear-modification factor, $R_{d\mathrm{Au}}$, as a function of p_T. The solid blue squares indicate the Au-going direction and the solid red circles indicate the d-going direction. The upright black triangles are for $\phi \to K^+K^-$ at midrapidity [36] while the inverted green triangles are for $\phi \to e^+e^-$. The vertical bars represent the statistical uncertainties and the boxes represent type-B systematic uncertainties. The ±13% global uncertainty is the associated type-C uncertainty.

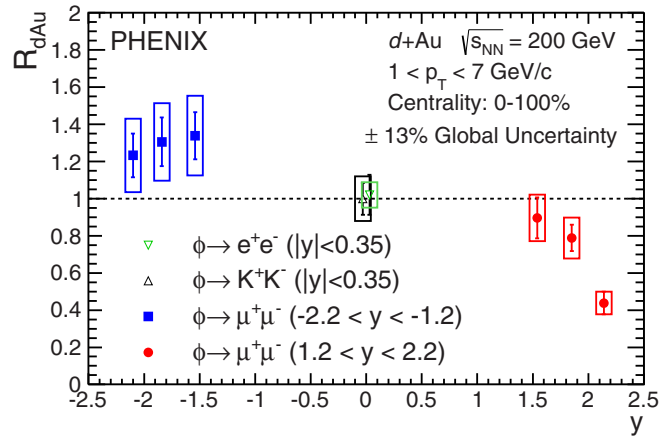

FIG. 9. (Color online) The ϕ meson nuclear modification factor, $R_{d\mathrm{Au}}$, as a function of rapidity. The solid blue squares indicate the Au-going direction, while the d-going direction is shown in solid red circles. At midrapidity, the upright black triangles are for $\phi \to K^+K^-$ [36], while the inverted green triangles are for $\phi \to e^+e^-$. The midrapidity points are slightly displaced from zero for clarity. The vertical bars represent the statistical uncertainties and the boxes represent type-B systematic uncertainties. The ±13% global uncertainty is the associated type-C uncertainty.

Figure 8 shows the $R_{d\mathrm{Au}}$ for ϕ mesons measured in all centralities as a function of p_T at forward and backward rapidities and at midrapidity, also compared with $R_{d\mathrm{Au}}$ measured in the $\phi \to K^+K^-$ decay channel [36]. The ϕ meson $R_{d\mathrm{Au}}$ behavior measured in the three different rapidity regions is not the same. In the Au-going direction, the $R_{d\mathrm{Au}}$ is consistent with unity at the lowest measured p_T and increases to $R_{d\mathrm{Au}} \sim 2$ at $p_T = 2.7$ GeV/c. It then decreases to unity at the highest measured p_T. In the d-going direction strong suppression is observed at the lowest measured p_T and then the $R_{d\mathrm{Au}}$ increases to unity at higher p_T. At midrapidity, where the measurement starts at $p_T = 0$, the yield of the ϕ meson is suppressed below 1 GeV/c and $R_{d\mathrm{Au}}$ is consistent with unity above that. The $R_{d\mathrm{Au}}$ measured in the $\phi \to K^+K^-$ channel agrees with the measurement of $\phi \to e^+e^-$ within uncertainties in the p_T region where the measurements overlap. The enhanced yield observed in the Au-going direction at intermediate p_T is characteristic of the Cronin effect [5]: enhancement of high-p_T particle production in d + Au collisions relative to scaled $p + p$ collisions with a corresponding depletion at low p_T. The ϕ enhancement in the Au-going direction and the suppression in the d-going direction are consistent with what is observed by ALICE in p + Pb collisions at $\sqrt{s_{NN}} = 5.02$ TeV in $-4.46 < y < -2.96$ and $2.03 < y < 3.53$ [54].

Figure 9 shows the $R_{d\mathrm{Au}}$ of the ϕ meson as a function of rapidity, summed over the p_T range $1 < p_T < 7$ GeV/c and integrated over all centralities. The $R_{d\mathrm{Au}}$ is enhanced in the Au-going direction, shows no modification at midrapidity, and is suppressed in the d-going direction.

Figure 10 shows that the ϕ meson nuclear modification factor, measured as a function of rapidity, is consistent with that of leptons coming from decays of heavy flavor particles [22,26]. This similarity is interesting given that heavy-flavor quark production is expected to be dominated by hard processes over the accessed p_T range. In contrast, one expects a significant contribution to ϕ meson production from soft processes, particularly at low p_T, where the yield is dominant. This backward (forward) enhancement (suppression) in d + Au collisions is also observed in d + Au charged hadron density results measured by PHOBOS [10]. The charged hadron result is often considered as a rapidity shift in the Au-going direction via soft processes.

Figure 10 also shows the J/ψ $R_{d\mathrm{Au}}$ [53]. In the case of the J/ψ, the relative $R_{d\mathrm{Au}}$ modification as a function of rapidity is similar to that of the ϕ meson and heavy-flavor decay leptons

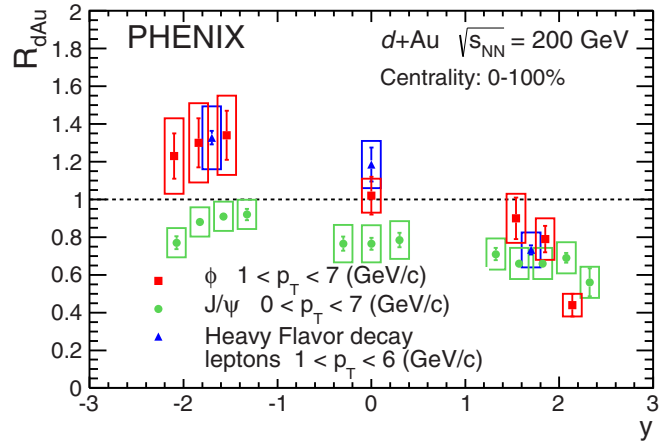

FIG. 10. (Color online) J/ψ [53] (solid green circles), heavy flavor decay leptons [22,26] (solid blue triangles), and ϕ meson (solid red squares) nuclear modification factors, $R_{d\mathrm{Au}}$, as functions of rapidity. The vertical bars represent the statistical uncertainties and the boxes represent type-B systematic uncertainties. The type-C systematic uncertainties associated with heavy-flavor and J/ψ meson measurements are 10% and 8%, respectively.

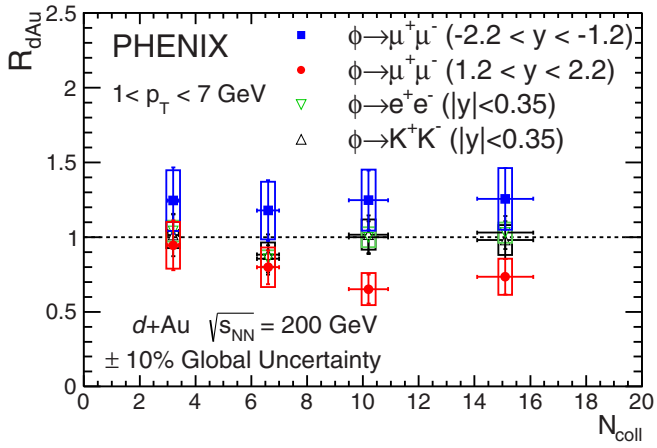

FIG. 11. (Color online) The ϕ meson nuclear modification factor, $R_{d\mathrm{Au}}$, as a function of N_{coll}. The solid blue squares indicate the Au-going direction, while the d-going direction is shown in solid red circles. At midrapidity, the upright black triangles are for $\phi \to K^+K^-$ [36], while the inverted green triangles are for $\phi \to e^+e^-$. The vertical bars represent the statistical uncertainties and the boxes represent type-B systematic uncertainties. The $\pm 10\%$ global uncertainty is the associated type-C uncertainty.

at forward rapidity. However, the J/ψ suffers from additional suppression at backward and midrapidity, which could be attributable to a larger break-up cross section or effects in the higher-energy-density backward-rapidity region.

At midrapidity, PHENIX measured the nuclear-modification factors of protons and of several mesons from the light (π) meson up to the ϕ meson with a mass similar to that of protons. The results show no significant dependence of $R_{d\mathrm{Au}}$ on the mass of the particle [24], whereas the measurements reveal a significant dependence of $R_{d\mathrm{Au}}$ on the number of valence quarks. All mesons show no or very small enhancement in comparison to protons in the low- to medium-p_T region.

Figure 11 shows the $R_{d\mathrm{Au}}$ integrated over the p_T range $1 < p_T < 7\ \mathrm{GeV}/c$ as a function of centrality for three rapidity intervals: $-2.2 < y < -1.2$, $1.2 < y < 2.2$, and $|y| < 0.35$. The $R_{d\mathrm{Au}}$ is integrated over the p_T range $1 < p_T < 7\ \mathrm{GeV}/c$ and the rapidity ranges $-2.2 < y < -1.2$, $1.2 < y < 2.2$, and $|y| < 0.35$. In the Au-going direction, the $R_{d\mathrm{Au}}$ shows an indication of enhancement with N_{coll} and in the d-going direction shows a strong suppression at high N_{coll}. At midrapidity, the $R_{d\mathrm{Au}}$ for ϕ mesons reconstructed in e^+e^- is consistent with unity at all centralities. This is also consistent with the measurement done in the K^+K^- decay channel.

Figure 12 shows $R_{d\mathrm{Au}}$ as a function of p_T in different d + Au centrality classes for three rapidity regions covered by the PHENIX detector: backward, mid, and forward rapidities. In the most peripheral collisions (60%–88%), shown in panel (d) of the figure, the nuclear-modification factor measured in all three rapidity regions is consistent with unity at all measured p_T. In the more central collisions the $R_{d\mathrm{Au}}$ remains at unity only in the midrapidity region for p_T above 1 GeV/c. This is consistent between the measurements done in the e^+e^- and in the K^+K^- decay channels. In the Au-going direction, the $R_{d\mathrm{Au}}$ reaches a maximum at p_T close to 2.7 GeV/c

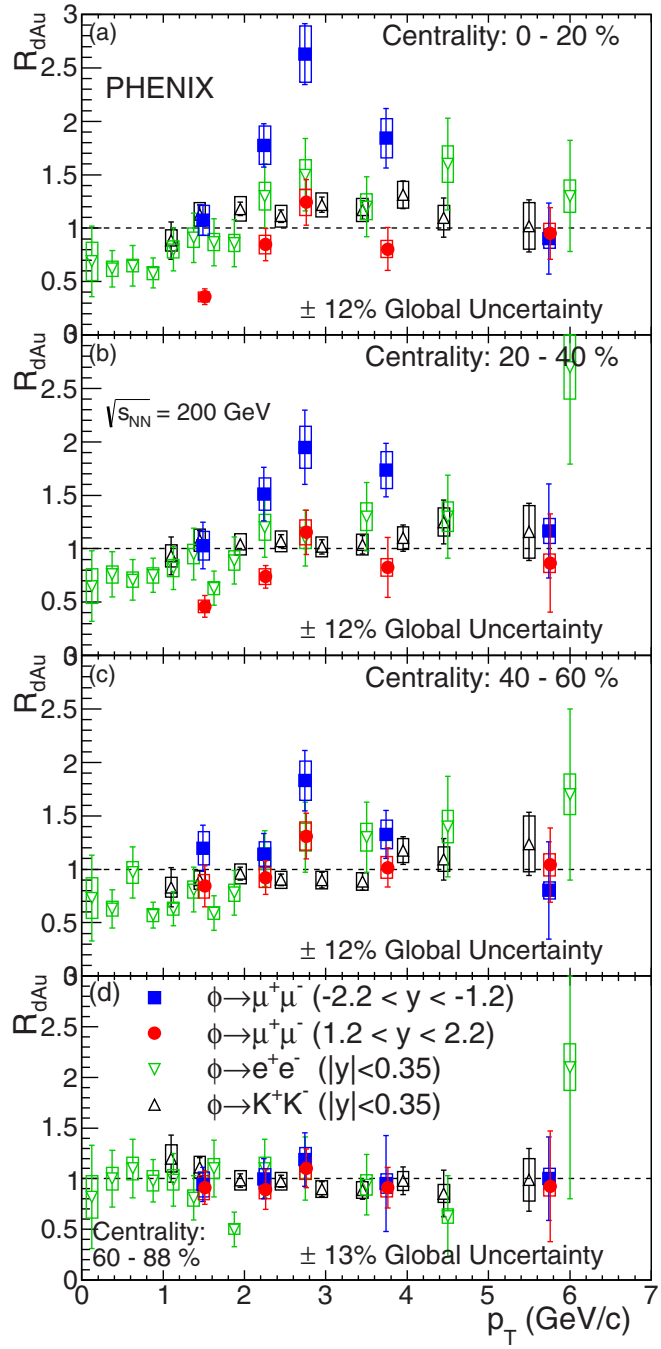

FIG. 12. (Color online) The ϕ meson $R_{d\mathrm{Au}}$ as a function of p_T for the centralities (a) 0%–20%, (b) 20%–40%, (c) 40%–60%, and (d) 60%–88% in the Au-going direction (solid blue squares) and the d-going direction (solid red circles). At midrapidity, the upright black triangles are from $\phi \to K^+K^-$ [36], while the inverted green triangles are from $\phi \to e^+e^-$. The vertical bars represent the statistical uncertainties and the boxes represent type-B systematic uncertainties. The $\pm 12\%$–13% global uncertainty is the associated type-C uncertainty.

with an amplitude that grows towards more central collisions. At higher p_T the $R_{d\mathrm{Au}}$ diminishes, approaching unity in all measured centrality classes. In the d-going direction, all points above 2.7 GeV/c are consistent with unity. Below $p_T =$

TABLE III. Invariant yields of ϕ meson production as a function of p_T at different d + Au centrality classes. The first uncertainty is statistical and the second is type-B systematic.

$p_T^{\min}$	$p_T^{\max}$	$\frac{B_{ll}}{2\pi p_T}\frac{d^2N}{dydp_T}$ (GeV/c)$^{-2}$				
(GeV/c)		0%–100%	0%–20%	20%–40%	40%–60%	60%–88%
				$-2.2 < y < -1.2$		
1.0	2.0	$(4.35 \pm 0.41 \pm 0.65)\times10^{-7}$	$(1.01 \pm 0.12 \pm 0.15)\times10^{-6}$	$(6.56 \pm 1.32 \pm 0.98)\times10^{-7}$	$(4.94 \pm 0.83 \pm 0.74)\times10^{-7}$	$(1.89 \pm 0.32 \pm 0.28)\times10^{-7}$
2.0	2.5	$(8.70 \pm 0.75 \pm 1.13)\times10^{-8}$	$(1.95 \pm 0.19 \pm 0.25)\times10^{-7}$	$(1.12 \pm 0.17 \pm 0.15)\times10^{-7}$	$(5.47 \pm 0.87 \pm 0.71)\times10^{-8}$	$(2.32 \pm 0.44 \pm 0.30)\times10^{-8}$
2.5	3.0	$(3.09 \pm 0.25 \pm 0.40)\times10^{-8}$	$(7.35 \pm 0.68 \pm 0.95)\times10^{-8}$	$(3.68 \pm 0.62 \pm 0.48)\times10^{-8}$	$(2.23 \pm 0.32 \pm 0.29)\times10^{-8}$	$(7.05 \pm 1.51 \pm 0.92)\times10^{-9}$
3.0	4.5	$(2.70 \pm 0.22 \pm 0.35)\times10^{-9}$	$(5.95 \pm 0.82 \pm 0.77)\times10^{-9}$	$(3.79 \pm 0.49 \pm 0.49)\times10^{-9}$	$(1.87 \pm 0.29 \pm 0.24)\times10^{-9}$	$(6.52 \pm 3.22 \pm 0.85)\times10^{-10}$
4.5	7.0	$(6.35 \pm 1.72 \pm 0.83)\times10^{-11}$	$(1.10 \pm 0.39 \pm 0.14)\times10^{-10}$	$(9.61 \pm 3.51 \pm 1.25)\times10^{-11}$	$(4.28 \pm 2.40 \pm 0.56)\times10^{-11}$	$(2.59 \pm 1.04 \pm 0.34)\times10^{-11}$
				$1.2 < y < 2.2$		
1.0	2.0	$(2.00 \pm 0.25 \pm 0.30)\times10^{-7}$	$(3.37 \pm 0.65 \pm 0.51)\times10^{-7}$	$(2.93 \pm 0.61 \pm 0.44)\times10^{-7}$	$(3.47 \pm 0.76 \pm 0.52)\times10^{-7}$	$(1.82 \pm 0.31 \pm 0.27)\times10^{-7}$
2.0	2.5	$(3.80 \pm 0.54 \pm 0.49)\times10^{-8}$	$(9.30 \pm 1.59 \pm 1.21)\times10^{-8}$	$(5.47 \pm 0.73 \pm 0.71)\times10^{-8}$	$(4.42 \pm 0.71 \pm 0.57)\times10^{-8}$	$(2.07 \pm 0.44 \pm 0.27)\times10^{-8}$
2.5	3.0	$(1.68 \pm 0.18 \pm 0.22)\times10^{-8}$	$(3.47 \pm 0.56 \pm 0.45)\times10^{-8}$	$(2.18 \pm 0.37 \pm 0.28)\times10^{-8}$	$(1.60 \pm 0.25 \pm 0.21)\times10^{-8}$	$(6.52 \pm 1.07 \pm 0.85)\times10^{-9}$
3.0	4.5	$(1.48 \pm 0.14 \pm 0.19)\times10^{-9}$	$(2.60 \pm 0.63 \pm 0.34)\times10^{-9}$	$(1.80 \pm 0.60 \pm 0.23)\times10^{-9}$	$(1.44 \pm 0.24 \pm 0.19)\times10^{-9}$	$(6.24 \pm 1.33 \pm 0.81)\times10^{-10}$
4.5	7.0	$(6.23 \pm 1.51 \pm 0.81)\times10^{-11}$	$(1.16 \pm 0.27 \pm 0.15)\times10^{-10}$	$(7.13 \pm 3.73 \pm 0.93)\times10^{-11}$	$(5.55 \pm 1.78 \pm 0.72)\times10^{-11}$	$(2.39 \pm 1.40 \pm 0.31)\times10^{-11}$
				$\lvert y \rvert < 0.35$		
0.00	0.25	$(9.81 \pm 2.88 \pm 3.01)\times10^{-6}$	$(1.93 \pm 0.76 \pm 0.55)\times10^{-5}$	$(1.23 \pm 0.53 \pm 0.33)\times10^{-5}$	$(8.92 \pm 4.22 \pm 2.42)\times10^{-6}$	$(4.87 \pm 2.74 \pm 1.26)\times10^{-6}$
0.25	0.50	$(7.18 \pm 0.74 \pm 1.57)\times10^{-6}$	$(1.23 \pm 0.22 \pm 0.23)\times10^{-5}$	$(1.03 \pm 0.16 \pm 0.22)\times10^{-5}$	$(5.46 \pm 1.02 \pm 1.05)\times10^{-6}$	$(4.28 \pm 0.81 \pm 0.81)\times10^{-6}$
0.50	0.75	$(3.49 \pm 0.35 \pm 0.71)\times10^{-6}$	$(6.11 \pm 1.00 \pm 1.30)\times10^{-6}$	$(4.52 \pm 0.69 \pm 0.90)\times10^{-6}$	$(3.96 \pm 0.54 \pm 0.69)\times10^{-6}$	$(2.18 \pm 0.36 \pm 0.39)\times10^{-6}$
0.75	1.00	$(2.19 \pm 0.18 \pm 0.42)\times10^{-6}$	$(3.54 \pm 0.46 \pm 0.70)\times10^{-6}$	$(3.13 \pm 0.36 \pm 0.58)\times10^{-6}$	$(1.54 \pm 0.20 \pm 0.25)\times10^{-6}$	$(1.28 \pm 0.17 \pm 0.22)\times10^{-6}$
1.00	1.25	$(1.18 \pm 0.09 \pm 0.21)\times10^{-6}$	$(2.16 \pm 0.24 \pm 0.40)\times10^{-6}$	$(1.51 \pm 0.17 \pm 0.27)\times10^{-6}$	$(7.44 \pm 1.13 \pm 1.21)\times10^{-7}$	$(5.70 \pm 0.93 \pm 0.93)\times10^{-7}$
1.25	1.50	$(6.20 \pm 0.49 \pm 1.08)\times10^{-7}$	$(1.26 \pm 0.14 \pm 0.22)\times10^{-6}$	$(8.92 \pm 0.99 \pm 1.51)\times10^{-7}$	$(4.87 \pm 0.67 \pm 0.77)\times10^{-7}$	$(2.37 \pm 0.38 \pm 0.39)\times10^{-7}$
1.50	1.75	$(2.75 \pm 0.24 \pm 0.46)\times10^{-7}$	$(6.32 \pm 0.78 \pm 1.08)\times10^{-7}$	$(3.13 \pm 0.45 \pm 0.51)\times10^{-7}$	$(1.90 \pm 0.30 \pm 0.30)\times10^{-7}$	$(1.65 \pm 0.26 \pm 0.27)\times10^{-7}$
1.75	2.00	$(1.59 \pm 0.15 \pm 0.26)\times10^{-7}$	$(3.31 \pm 0.43 \pm 0.55)\times10^{-7}$	$(2.34 \pm 0.30 \pm 0.37)\times10^{-7}$	$(1.32 \pm 0.21 \pm 0.21)\times10^{-7}$	$(4.11 \pm 1.03 \pm 0.67)\times10^{-8}$
2.00	2.50	$(9.22 \pm 0.62 \pm 1.48)\times10^{-8}$	$(2.01 \pm 0.18 \pm 0.32)\times10^{-7}$	$(1.29 \pm 0.12 \pm 0.20)\times10^{-7}$	$(7.15 \pm 0.85 \pm 1.13)\times10^{-8}$	$(3.60 \pm 0.56 \pm 0.59)\times10^{-8}$
2.50	3.00	$(3.19 \pm 0.24 \pm 0.49)\times10^{-8}$	$(7.12 \pm 0.71 \pm 1.10)\times10^{-8}$	$(3.54 \pm 0.44 \pm 0.53)\times10^{-8}$	$(2.84 \pm 0.39 \pm 0.44)\times10^{-8}$	$(1.10 \pm 0.22 \pm 0.18)\times10^{-8}$
3.00	4.00	$(6.17 \pm 0.49 \pm 0.94)\times10^{-9}$	$(1.15 \pm 0.14 \pm 0.18)\times10^{-8}$	$(8.92 \pm 1.10 \pm 1.36)\times10^{-9}$	$(5.52 \pm 0.81 \pm 0.88)\times10^{-9}$	$(1.94 \pm 0.44 \pm 0.33)\times10^{-9}$
4.00	5.00	$(9.45 \pm 1.25 \pm 1.47)\times10^{-10}$	$(2.27 \pm 0.37 \pm 0.37)\times10^{-9}$	$(1.27 \pm 0.26 \pm 0.20)\times10^{-9}$	$(8.74 \pm 2.06 \pm 1.57)\times10^{-10}$	$(1.87 \pm 1.10 \pm 0.34)\times10^{-10}$
5.00	7.00	$(1.02 \pm 0.19 \pm 0.17)\times10^{-10}$	$(1.46 \pm 0.45 \pm 0.25)\times10^{-10}$	$(1.98 \pm 0.50 \pm 0.03)\times10^{-10}$	$(8.27 \pm 3.16 \pm 1.59)\times10^{-11}$	$(4.79 \pm 2.74 \pm 0.90)\times10^{-11}$

TABLE IV. $R_{d\mathrm{Au}}$ as a function of rapidity of ϕ meson summed over the p_T range, $1 < p_T < 7$ GeV/c for 0%–100% centrality. The first uncertainty is statistical and the second is type-B systematic.

y_{min}	y_{max}	$R_{d\mathrm{Au}}$
–2.2	−2.0	$1.23 \pm 0.12 \pm 0.20$
–2.0	−1.7	$1.30 \pm 0.13 \pm 0.21$
–1.7	−1.1	$1.34 \pm 0.13 \pm 0.21$
–0.35	0.35	$1.02 \pm 0.11 \pm 0.07$
1.2	1.7	$0.90 \pm 0.11 \pm 0.13$
1.7	2.0	$0.79 \pm 0.07 \pm 0.11$
2.0	2.2	$0.44 \pm 0.06 \pm 0.06$

2.7 GeV/c, Fig. 12 shows $R_{d\mathrm{Au}} < 1$, with more suppression in the most central collisions compared to other centralities.

The enhancement at backward rapidity is consistent with nuclear p_T broadening at moderate p_T and gluon antishadowing, while the suppression at forward rapidity may suggest gluon shadowing and/or partonic energy loss. The $R_{d\mathrm{Au}}$ enhancement (suppression) at backward (forward) rapidity in the most central collisions decreases gradually from central to peripheral collisions where for the most peripheral collisions $R_{d\mathrm{Au}}$ shows no overall modification. Whether the ϕ meson is dominated by soft or hard processes remains an open question.

V. SUMMARY AND CONCLUSIONS

PHENIX has measured the production of ϕ mesons in d + Au collisions at $\sqrt{s_{NN}} = 200$ GeV via their decay to dimuons and dielectrons. The ϕ meson is measured in the forward, d-going direction, $1.2 < y < 2.2$ in the p_T range from 1 to 7 GeV/c, at midrapidity $|y| < 0.35$ in the p_T range below 7 GeV/c, and in the backward, the Au-going direction, $-2.2 < y < -1.2$ in the p_T range from 1 to 7 GeV/c.

The measurements reveal that the ϕ meson yields in d + Au compared to binary collision scaled $p + p$ at $p_T > 2$ GeV/c are suppressed in the d-going direction and enhanced in the Au-going direction. The yield measured at midrapidity is consistent with binary collision scaled $p + p$. No significant modification of ϕ meson production is observed in the most peripheral d + Au collisions. With centrality increasing from semiperipheral events to central, the $R_{d\mathrm{Au}}$ shows more pronounced suppression in the d-going direction and more increasing enhancement in Au-going direction. In that rapidity region, the $R_{d\mathrm{Au}}$ has a p_T dependence, which is characteristic of a Cronin-type effect. A similar enhancement (suppression) was observed by ALICE in p + Pb collisions at $\sqrt{s_{NN}} = 5.02$ TeV [54]. The rapidity dependence of the $R_{d\mathrm{Au}}$ in ϕ meson production is similar to the open heavy flavor modification [26], which may indicate a general rapidity shift compared to the symmetric system and/or similar cold-nuclear-matter effects are present in both the ϕ meson and open heavy-flavor production.

ACKNOWLEDGMENTS

We thank the staff of the Collider-Accelerator and Physics Departments at Brookhaven National Laboratory and the staff of the other PHENIX participating institutions for their vital contributions. We acknowledge support from the Office of Nuclear Physics in the Office of Science of the Department of Energy, the National Science Foundation, Abilene Christian University Research Council, Research Foundation of SUNY, and Dean of the College of Arts and Sciences, Vanderbilt University (U.S.A); Ministry of Education, Culture, Sports, Science, and Technology and the Japan Society for the Promotion of Science (Japan); Conselho Nacional de Desenvolvimento Científico e Tecnológico and Fundação de Amparo à Pesquisa do Estado de São Paulo (Brazil); Natural Science Foundation of China (Pople's Republic of China); Ministry of Science, Education, and Sports (Croatia); Ministry of Education, Youth and Sports (Czech Republic); Centre National de la Recherche Scientifique, Commissariat à l'Énergie Atomique, and Institut National de Physique Nucléaire et de Physique des Particules (France); Bundesministerium für Bildung und Forschung, Deutscher Akademischer Austausch Dienst, and Alexander von Humboldt Stiftung (Germany); National Science Fund, OTKA, Károly Róbert University College, and the Ch. Simonyi Fund (Hungary); Department of Atomic Energy and Department of Science and Technology (India); Israel Science Foundation (Israel); Basic Science Research Program through NRF of the Ministry of Education (Korea); Physics Department, Lahore University of Management Sciences (Pakistan); Ministry of Education and Science, Russian Academy of Sciences, Federal Agency of Atomic Energy (Russia); VR and Wallenberg Foundation (Sweden); the U.S. Civilian Research and Development Foundation for the Independent States of the Former Soviet Union, the Hungarian American Enterprise Scholarship Fund, and the US-Israel Binational Science Foundation.

APPENDIX

Tables III–VI show the numerical values of the measured invariant yields and $R_{d\mathrm{Au}}$ that are plotted in Figs. 6–12. As noted in each caption, the first uncertainty is statistical and the second is type-B systematic.

TABLE V. $R_{d\mathrm{Au}}$ vs N_{coll} of ϕ meson at $1 < p_T < 7$ GeV/c. The first uncertainty is statistical and the second is type-B systematic.

Centrality (%)	$\langle N_{\mathrm{coll}} \rangle$	$R_{d\mathrm{Au}}$		
		$-2.2 < y < -1.2$	$1.2 < y < 2.2$	$\lvert y \rvert < 0.35$
0–20	15.1 ± 1.0	$1.26 \pm 0.21 \pm 0.21$	$0.73 \pm 0.12 \pm 0.12$	$1.03 \pm 0.11 \pm 0.09$
20–40	10.2 ± 0.7	$1.25 \pm 0.20 \pm 0.20$	$0.65 \pm 0.10 \pm 0.11$	$1.00 \pm 0.10 \pm 0.09$
40–60	6.6 ± 0.4	$1.18 \pm 0.20 \pm 0.19$	$0.80 \pm 0.11 \pm 0.13$	$0.86 \pm 0.09 \pm 0.08$
60–88	3.2 ± 0.2	$1.24 \pm 0.22 \pm 0.20$	$0.95 \pm 0.17 \pm 0.16$	$1.04 \pm 0.11 \pm 0.09$

TABLE VI. $R_{d\mathrm{Au}}$ and p_T at different d + Au centrality classes. The first uncertainty is statistical and the second is type-B systematic.

$p_T^{\min}$	$p_T^{\max}$	$R_{d\mathrm{Au}}$				
(GeV/c)		0%–100%	0%–20%	20%–40%	40%–60%	60%–88%
				$-2.2 < y < -1.2$		
1.0	2.0	0.92 ± 0.10 ± 0.12	1.07 ± 0.14 ± 0.14	1.03 ± 0.22 ± 0.13	1.20 ± 0.22 ± 0.16	0.94 ± 0.17 ± 0.12
2.0	2.5	1.57 ± 0.16 ± 0.19	1.78 ± 0.20 ± 0.18	1.51 ± 0.25 ± 0.15	1.14 ± 0.19 ± 0.11	1.00 ± 0.20 ± 0.10
2.5	3.0	2.19 ± 0.22 ± 0.26	2.63 ± 0.29 ± 0.26	1.95 ± 0.35 ± 0.19	1.83 ± 0.28 ± 0.18	1.19 ± 0.26 ± 0.12
3.0	4.5	1.66 ± 0.17 ± 0.20	1.84 ± 0.28 ± 0.18	1.74 ± 0.25 ± 0.17	1.33 ± 0.22 ± 0.13	0.95 ± 0.47 ± 0.10
4.5	7.0	1.03 ± 0.30 ± 0.12	0.90 ± 0.33 ± 0.09	1.17 ± 0.44 ± 0.12	0.80 ± 0.46 ± 0.08	1.00 ± 0.41 ± 0.10
				$1.2 < y < 2.2$		
1.0	2.0	0.42 ± 0.06 ± 0.05	0.36 ± 0.07 ± 0.05	0.46 ± 0.10 ± 0.06	0.84 ± 0.19 ± 0.11	0.91 ± 0.16 ± 0.12
2.0	2.5	0.69 ± 0.10 ± 0.08	0.85 ± 0.15 ± 0.08	0.74 ± 0.11 ± 0.07	0.92 ± 0.16 ± 0.09	0.89 ± 0.20 ± 0.09
2.5	3.0	1.20 ± 0.14 ± 0.13	1.24 ± 0.21 ± 0.12	1.15 ± 0.21 ± 0.12	1.31 ± 0.22 ± 0.13	1.10 ± 0.19 ± 0.11
3.0	4.5	0.91 ± 0.10 ± 0.10	0.80 ± 0.20 ± 0.08	0.83 ± 0.28 ± 0.08	1.02 ± 0.18 ± 0.10	0.91 ± 0.20 ± 0.09
4.5	7.0	1.01 ± 0.26 ± 0.11	0.95 ± 0.24 ± 0.10	0.87 ± 0.46 ± 0.09	1.04 ± 0.35 ± 0.10	0.92 ± 0.55 ± 0.09
				$\|y\| < 0.35$		
0.00	0.25	0.70 ± 0.29 ± 0.18	0.69 ± 0.33 ± 0.18	0.65 ± 0.33 ± 0.16	0.73 ± 0.40 ± 0.19	0.82 ± 0.51 ± 0.21
0.25	0.50	0.72 ± 0.18 ± 0.08	0.62 ± 0.17 ± 0.07	0.76 ± 0.21 ± 0.08	0.63 ± 0.18 ± 0.07	1.00 ± 0.28 ± 0.11
0.50	0.75	0.74 ± 0.18 ± 0.07	0.65 ± 0.19 ± 0.06	0.71 ± 0.19 ± 0.07	0.97 ± 0.24 ± 0.10	1.10 ± 0.29 ± 0.11
0.75	1.00	0.71 ± 0.15 ± 0.07	0.58 ± 0.14 ± 0.06	0.75 ± 0.16 ± 0.07	0.57 ± 0.12 ± 0.06	0.98 ± 0.21 ± 0.10
1.00	1.25	0.86 ± 0.20 ± 0.09	0.80 ± 0.20 ± 0.08	0.82 ± 0.20 ± 0.08	0.63 ± 0.16 ± 0.06	0.99 ± 0.26 ± 0.10
1.25	1.50	0.89 ± 0.22 ± 0.09	0.91 ± 0.23 ± 0.09	0.95 ± 0.24 ± 0.09	0.81 ± 0.21 ± 0.08	0.81 ± 0.22 ± 0.08
1.50	1.75	0.75 ± 0.18 ± 0.07	0.87 ± 0.22 ± 0.08	0.63 ± 0.16 ± 0.06	0.60 ± 0.16 ± 0.06	1.10 ± 0.28 ± 0.10
1.75	2.00	0.82 ± 0.19 ± 0.08	0.86 ± 0.22 ± 0.08	0.89 ± 0.22 ± 0.09	0.78 ± 0.21 ± 0.08	0.50 ± 0.17 ± 0.05
2.00	2.50	1.20 ± 0.26 ± 0.12	1.30 ± 0.30 ± 0.13	1.20 ± 0.28 ± 0.12	1.10 ± 0.26 ± 0.10	1.10 ± 0.29 ± 0.11
2.50	3.00	1.30 ± 0.29 ± 0.13	1.50 ± 0.34 ± 0.14	1.10 ± 0.26 ± 0.10	1.30 ± 0.33 ± 0.13	1.10 ± 0.31 ± 0.10
3.00	4.00	1.20 ± 0.27 ± 0.13	1.20 ± 0.28 ± 0.12	1.30 ± 0.32 ± 0.13	1.30 ± 0.33 ± 0.13	0.94 ± 0.30 ± 0.09
4.00	5.00	1.30 ± 0.33 ± 0.14	1.60 ± 0.43 ± 0.17	1.30 ± 0.39 ± 0.14	1.40 ± 0.47 ± 0.15	0.63 ± 0.40 ± 0.07
5.00	7.00	1.80 ± 0.54 ± 0.21	1.30 ± 0.52 ± 0.15	2.70 ± 0.91 ± 0.30	1.70 ± 0.80 ± 0.19	2.10 ± 1.30 ± 0.23

[1] K. Adcox *et al.* (PHENIX Collaboration), Formation of dense partonic matter in relativistic nucleus-nucleus collisions at RHIC: Experimental evaluation by the PHENIX Collaboration, Nucl. Phys. A **757**, 184 (2005).

[2] J. Adams *et al.* (STAR Collaboration), Experimental and theoretical challenges in the search for the quark gluon plasma: The STAR Collaboration's critical assessment of the evidence from RHIC collisions, Nucl. Phys. A **757**, 102 (2005).

[3] J. J. Heckman, J. Seo, and C. Vafa, Phase structure of a brane/anti-brane system at large N, J. High Energy Phys. 07 (2007) 073.

[4] I. Vitev, Initial state parton broadening and energy loss probed in d+Au at RHIC, Phys. Lett. B **562**, 36 (2003).

[5] J. W. Cronin, H. J. Frisch, M. J. Shochet, J. P. Boymond, R. Mermod, *et al.*, Production of Hadrons with Large Transverse Momentum at 200 GeV, 300 GeV, and 400 GeV, Phys. Rev. D **11**, 3105 (1975).

[6] A. Accardi and M. Gyulassy, Cronin effect versus geometrical shadowing in d + Au collisions at RHIC, Phys. Lett. B **586**, 244 (2004).

[7] A. Adare *et al.* (PHENIX Collaboration), Quadrupole Anisotropy in Dihadron Azimuthal Correlations in Central d + Au Collisions at $\sqrt{s_{NN}} = 200$ GeV, Phys. Rev. Lett. **111**, 212301 (2013).

[8] A. Adare *et al.* (PHENIX Collaboration), Measurement of Long-Range Angular Correlation and Quadrupole Anisotropy of Pions and (Anti)protons in Central d + Au Collisions at $\sqrt{s_{NN}} = 200$ GeV, Phys. Rev. Lett. **114**, 192301 (2015).

[9] B. B. Back *et al.* (PHOBOS Collaboration), Pseudorapidity Distribution of Charged Particles in d + Au Collisions at $\sqrt{s_{NN}} = 200$ GeV, Phys. Rev. Lett. **93**, 082301 (2004).

[10] B. B. Back *et al.* (PHOBOS Collaboration), Scaling of charged particle production in d + Au collisions at $\sqrt{s_{NN}} = 200$ GeV, Phys. Rev. C **72**, 031901 (2005).

[11] I. Arsene *et al.* (BRAHMS Collaboration), Centrality Dependence of Charged-Particle Pseudorapidity Distributions from d + Au Collisions at $\sqrt{s_{NN}} = 200$ GeV, Phys. Rev. Lett. **94**, 032301 (2005).

[12] B. I. Abelev *et al.* (STAR Collaboration), Systematic measurements of identified particle spectra in pp, d + Au, and Au + Au collisions at the STAR detector, Phys. Rev. C **79**, 034909 (2009).

[13] S. Chatrchyan *et al.* (CMS Collaboration), Observation of long-range near-side angular correlations in proton-lead collisions at the LHC, Phys. Lett. B **718**, 795 (2013).

[14] G. Aad *et al.* (ATLAS Collaboration), Observation of Associated Near-Side and Away-Side Long-Range Correlations in $\sqrt{s_{NN}} = 5.02$ TeV Proton-Lead Collisions with the ATLAS Detector, Phys. Rev. Lett. **110**, 182302 (2013).

[15] S. Chatrchyan *et al.* (CMS Collaboration), Multiplicity and transverse momentum dependence of two- and four-particle correlations in *p*Pb and PbPb collisions, Phys. Lett. B **724**, 213 (2013).

[16] G. Aad *et al.* (ATLAS Collaboration), Measurement with the ATLAS detector of multi-particle azimuthal correlations in $p+$ Pb collisions at $\sqrt{s_{NN}} = 5.02$ TeV, Phys. Lett. B **725**, 60 (2013).

[17] B. B. Abelev *et al.* (ALICE Collaboration), Long-range angular correlations of π, K, and p in p-Pb collisions at $\sqrt{s_{NN}} = 5.02$ TeV, Phys. Lett. B **726**, 164 (2013).

[18] G. Aad *et al.* (ATLAS Collaboration), Measurement of long-range pseudorapidity correlations and azimuthal harmonics in $\sqrt{s_{NN}} = 5.02$ TeV proton-lead collisions with the ATLAS detector, Phys. Rev. C **90**, 044906 (2014).

[19] B. B. Abelev *et al.* (ALICE Collaboration), Multiparticle azimuthal correlations in p-Pb and Pb-Pb collisions at the CERN Large Hadron Collider, Phys. Rev. C **90**, 054901 (2014).

[20] L. Adamczyk *et al.* (STAR Collaboration), Long-range pseudorapidity dihadron correlations in $d+$ Au collisions at $\sqrt{s_{NN}} =$ 5.02 GeV, Phys. Lett. B **747**, 265 (2015).

[21] A. Adare *et al.* (PHENIX Collaboration), Transverse-momentum dependence of the J/ψ nuclear modification in $d+$ Au collisions at $\sqrt{s_{NN}} = 200$ GeV, Phys. Rev. C **87**, 034904 (2013).

[22] A. Adare *et al.* (PHENIX Collaboration), Cold-Nuclear-Matter Effects on Heavy-Quark Production in $d+$ Au Collisions at $\sqrt{s_{NN}} = 200$ GeV, Phys. Rev. Lett. **109**, 242301 (2012).

[23] A. Adare *et al.* (PHENIX Collaboration), $\Upsilon(1S+2S+3S)$ production in $d+$ Au and $p+p$ collisions at $\sqrt{s_{NN}} = 200$ GeV and cold-nuclear matter effects, Phys. Rev. C **87**, 044909 (2013).

[24] A. Adare *et al.* (PHENIX Collaboration), Spectra and ratios of identified particles in Au + Au and $d+$ Au collisions at $\sqrt{s_{NN}} = 200$ GeV, Phys. Rev. C **88**, 024906 (2013).

[25] A. Adare *et al.* (PHENIX Collaboration), Nuclear Modification of ψ', χ_c, and J/ψ Production in $d+$ Au Collisions at $\sqrt{s_{NN}} =$ 200 GeV, Phys. Rev. Lett. **111**, 202301 (2013).

[26] A. Adare *et al.* (PHENIX Collaboration), Cold-Nuclear-Matter Effects on Heavy-Quark Production at Forward and Backward Rapidity in $d+$ Au Collisions at $\sqrt{s_{NN}} = 200$ GeV, Phys. Rev. Lett. **112**, 252301 (2014).

[27] P. Koch, B. Muller, and J. Rafelski, Strangeness in relativistic heavy ion collisions, Phys. Rep. **142**, 167 (1986).

[28] A. Shor, φ Meson Production as a Probe of the Quark Gluon Plasma, Phys. Rev. Lett. **54**, 1122 (1985).

[29] B. Alessandro *et al.* (NA50 Collaboration), φ production in Pb-Pb collisions at 158 GeV/c per nucleon incident momentum, Phys. Lett. B **555**, 147 (2003).

[30] S. S. Adler *et al.* (PHENIX Collaboration), Production of ϕ mesons at mid-rapidity in $\sqrt{s_{NN}} = 200$ GeV Au + Au collisions at RHIC, Phys. Rev. C **72**, 014903 (2005).

[31] S. Afanasiev *et al.* (PHENIX Collaboration), Elliptic Flow for ϕ Mesons and (Anti)deuterons in Au + Au Collisions at $\sqrt{s_{NN}} =$ 200 GeV, Phys. Rev. Lett. **99**, 052301 (2007).

[32] B. I. Abelev *et al.* (STAR Collaboration), Partonic Flow and ϕ-Meson Production in Au + Au Collisions at $\sqrt{s_{NN}} =$ 200 GeV, Phys. Rev. Lett. **99**, 112301 (2007).

[33] D. Adamova *et al.* (CERES Collaboration), Modification of the rho-meson detected by low-mass electron-positron pairs in central Pb-Au collisions at 158-A GeV/c, Phys. Lett. B **666**, 425 (2008).

[34] C. Alt *et al.* (NA49 Collaboration), Energy dependence of ϕ meson production in central Pb+Pb collisions at $\sqrt{s_{NN}} = 6$ to 17 GeV, Phys. Rev. C **78**, 044907 (2008).

[35] B. I. Abelev *et al.* (STAR Collaboration), Energy and system size dependence of ϕ meson production in Cu + Cu and Au + Au collisions, Phys. Lett. B **673**, 183 (2009).

[36] A. Adare *et al.* (PHENIX Collaboration), Nuclear modification factors of ϕ mesons in $d+$ Au, Cu + Cu and Au + Au collisions at $\sqrt{s_{NN}} = 200$ GeV, Phys. Rev. C **83**, 024909 (2011).

[37] R. Arnaldi *et al.* (NA60 Collaboration), A Comparative measurement of $\phi \to K^+K^-$ and $\phi \to \mu^+\mu^-$ in In-In collisions at the CERN SPS, Phys. Lett. B **699**, 325 (2011).

[38] A. Adare *et al.* (PHENIX Collaboration), Measurement of neutral mesons in $p+p$ collisions at $\sqrt{s} = 200$ GeV and scaling properties of hadron production, Phys. Rev. D **83**, 052004 (2011).

[39] A. Adare *et al.* (PHENIX Collaboration), Low-mass vector-meson production at forward rapidity in $p+p$ collisions at $\sqrt{s} = 200$ GeV, Phys. Rev. D **90**, 052002 (2014).

[40] K. Adcox *et al.* (PHENIX Collaboration), PHENIX detector overview, Nucl. Instrum. Methods Phys. Res., Sect. A **499**, 469 (2003).

[41] J. Beringer *et al.* (Particle Data Group), Review of Particle Phys. (RPP), Phys. Rev. D **86**, 010001 (2012).

[42] W. M. Yao *et al.* (Particle Data Group), Review of Particle Physics, J. Phys. G **33**, 1 (2006).

[43] T. Sjostrand, P. Eden, C. Friberg, L. Lonnblad, G. Miu, S. Mrenna, and E. Norrbin, High-energy physics event generation with PYTHIA 6.1, Comput. Phys. Commun. **135**, 238 (2001).

[44] *GEANT 3.2.1 Manual* (1994), CERN W5013.

[45] A. Adare *et al.* (PHENIX Collaboration), Production of ω mesons in $p+p$, $d+$ Au, Cu + Cu, and Au + Au collisions at $\sqrt{s_{NN}} = 200$ GeV, Phys. Rev. C **84**, 044902 (2011).

[46] A. Adare *et al.* (PHENIX Collaboration), Detailed measurement of the e^+e^- pair continuum in $p+p$ and Au + Au collisions at $\sqrt{s_{NN}} = 200$ GeV and implications for direct photon production, Phys. Rev. C **81**, 034911 (2010).

[47] A. Adare *et al.* (PHENIX Collaboration), Centrality categorization for $R_{p(d)+A}$ in high-energy collisions, Phys. Rev. C **90**, 034902 (2014).

[48] S. S. Adler *et al.* (PHENIX Collaboration), J/ψ Production and Nuclear Effects for $d+$ Au and $p+p$ Collisions at $\sqrt{s_{NN}} =$ 200 GeV, Phys. Rev. Lett. **96**, 012304 (2006).

[49] G. D. Lafferty and T.R. Wyatt, Where to stick your data points: The treatment of measurements within wide bins, Nucl. Instrum. Methods Phys. Res., Sect. A **355**, 541 (1995).

[50] R. Hagedorn, Statistical thermodynamics of strong interactions at high-energies, Nuovo Cim. Suppl. **3**, 147 (1965).

[51] D. M. Kaplan *et al.* (FNAL-E288 Collaboration), Study of the High Mass Dimuon Continuum in 400 GeV Proton-Nucleus Collisions, Phys. Rev. Lett. **40**, 435 (1978).

[52] C. Tsallis, Possible Generalization of Boltzmann-Gibbs Statistics, J. Stat. Phys. **52**, 479 (1988).

[53] A. Adare *et al.* (PHENIX Collaboration), Cold Nuclear Matter Effects on J/ψ Yields as a Function of Rapidity and Nuclear Geometry in Deuteron-Gold Collisions at $\sqrt{s_{NN}} = 200$ GeV, Phys. Rev. Lett. **107**, 142301 (2011).

[54] J. Adam *et al.* (ALICE Collaboration), ϕ-meson production at forward rapidity in $p+Pb$ collisions at $\sqrt{s_{NN}} = 5.02$ TeV and in $p+p$ collisions at $\sqrt{s} = 2.86$ TeV, arXiv:1506.09206.